

Polycontinuous geometries for inverse lipid phases with more than two aqueous network domains

Gerd E. Schröder-Turk,^{a,*;‡} Liliana de Campo,^{c;‡} Myfanwy E. Evans,^a Matthias Saba,^a Sebastian Kapfer,^a Trond Varslot,^c Karsten Grosse-Brauckmann,^b Stuart Ramsden,^c and Stephen Hyde^c

Received 31st May 2012

Inverse bicontinuous cubic phases with *two* aqueous network domains separated by a smooth bilayer are firmly established as equilibrium phases in lipid/water systems. The purpose of this article is to highlight generalisations of these bicontinuous geometries to polycontinuous geometries, which could be realised as lipid mesophases with three or more network-like aqueous domains separated by a branched bilayer. An analysis of structural homogeneity in terms of bilayer width variations reveals that ordered polycontinuous geometries are likely candidates for lipid mesophase structures, with similar chain packing characteristics to inverse micellar phases (that once were believed not to exist due to high packing frustration). The average molecular shape required by global geometry to form these multi-network phases is quantified by the surfactant shape parameter $v/(al)$; we find that it adopts values close to those of the known lipid phases. We specifically analyse the **3etc**(187,193) structure of hexagonal symmetry $P6_3/mcm$ with three aqueous domains, the **3dia**(24,220) structure of cubic symmetry $I\bar{4}3d$ composed of three distorted Diamond networks, the cubic chiral **4srs***(24,208) with cubic symmetry $P4_232$ and the achiral **4srs**(5,133) structure of symmetry $P4_2/nbc$, each consisting of four intergrown undistorted copies of the **srs** net (the same net as in the Q_{II}^G Gyroid phase). Structural homogeneity is analysed by a medial surface approach assuming that the head group interfaces are constant mean curvature surfaces. To facilitate future experimental identification, we provide simulated SAXS scattering patterns that, for the **4srs***(24,208) and **3dia**(24,220) structures, bear remarkable similarity to those of bicontinuous Q_{II}^G -Gyroid and Q_{II}^D -Diamond phases, with comparable lattice parameters and only a single peak that cannot be indexed to the well-established structures. While polycontinuous lipid phases have to date not been reported, the likelihood of their formation is further indicated by the reported observation of a solid tricontinuous mesoporous silicate structure termed IBN-9 formed in the presence of surfactants [Han *et al.*, *Nat. Chem.*, 2009, **1**, 123].

^a Theoretische Physik I, Friedrich-Alexander Universität Erlangen-Nürnberg, Staudtstr. 7B, Erlangen, Germany.

* Corresponding author. E-mail: gerd.schroeder-turk@physik.uni-erlangen.de

^b Fachbereich Mathematik, Technische Universität Darmstadt, Schlossgartenstr. 7, 64289 Darmstadt, Germany

^c Applied Maths, Research School of Physical Sciences & Engineering, Australian National University, 0200 ACT, Australia

‡ GEST and LDC have contributed equally to the work described in this article.

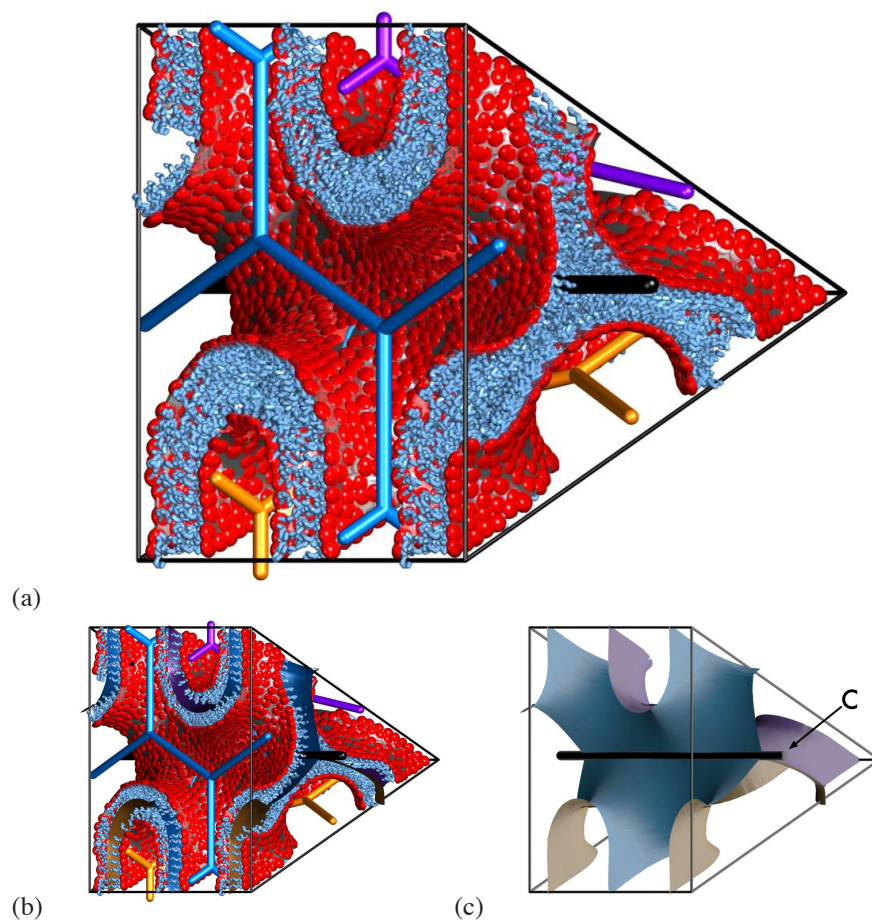


Fig. 1 (a) Artist's impression of the hypothetical inverse tricontinuous $3etc(187,193)$ lipid phase geometry. The structure is composed of three aqueous domains (blue, purple and orange nets) each of which has a network-like shape centred on a periodic hexagonal **etc** net. These aqueous domains are separated by a lipid bilayer which, similar to the bilayer in the inverse hexagonal columnar phase H_{II} , is branched. The bilayer mid-surface, illustrated in (b) and (c), is a branched and warped surface that consists in smooth surface patches and triple branch-lines where three surface patches meet at 120° degree angles (black line along the crystallographic c axis).

1 Introduction

The existence of bicontinuous cubic phases in lipid systems is now widely accepted, based on studies in the 1960's through 1990's¹⁻⁷. Of particular interest are the inverse (or type II) bicontinuous cubic phases Q_{II}^G (of cubic symmetry $Ia\bar{3}d$), Q_{II}^D ($Pn\bar{3}m$) and Q_{II}^P ($Im\bar{3}m$) where the spatial structure is a lipid bilayer draped onto a triply-periodic minimal surface; the aqueous domain consists of two network-like components, separated by the bilayer, see Fig. 2. While a large range of triply-periodic minimal surfaces of various topology and symmetry ex-

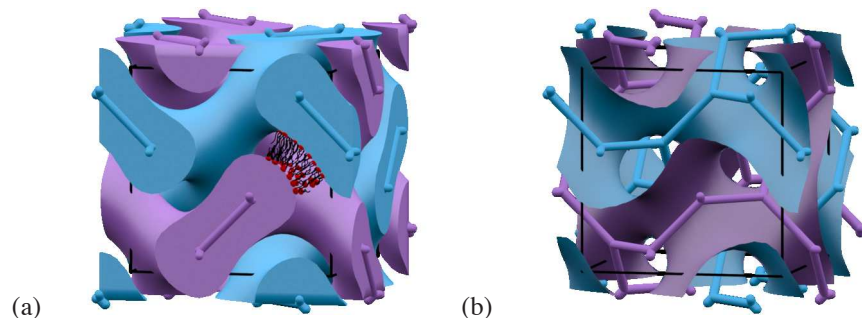


Fig. 2 Geometry of the conventional $Ia\bar{3}d$ inverse bicontinuous Q_{II}^G phase, based on the $2srs(230,214)$ nets: (a) Two aqueous domains, given by CMC surfaces centred on two (enantiomeric) srs nets, are separated by a lipid bilayer. (b) The medial surface representing the mid-surface of the bilayer is the same as the minimal $H = 0$ Gyroid surface of symmetry $Ia\bar{3}d$, within numerical accuracy. For clarity, the CMC surfaces bounding the two aqueous domains are displayed with different colours; in the mesophases described here the aqueous domains are indistinguishable.

ist, only three cubic examples are ubiquitously found in lipid self-assembly and related systems such as copolymers; these are the (G)yroid⁸, the (D)iamond⁹ and the (P)rimitive⁹ that lend their structure to the Q_{II}^G , Q_{II}^D and Q_{II}^P lipid phases. The geometry described by a minimal surface is termed *bicontinuous* if the surface divides space into two interpenetrating network-like sub-volumes, each of which is a single connected component (i.e. mathematically, *continuous*), in contrast to e.g. the aqueous phase in the inverse micellar Q_{II}^{227} phase that consists in many disconnected globules¹⁰; the geometry of the network-like aqueous domains is conveniently characterised by the centred skeletal graph or net, see Fig. 2.

The second characteristic feature of the inverse bicontinuous phases is the fact that they form smooth and homogeneous manifold surfaces with very small degree of spatial variation in terms of surface curvatures^{11,12} and also channel diameters^{13,14} – properties that relate to the free energies of the self-assembled systems through the concepts of bending rigidity, packing frustration and chain stretching^{15–17}.

This article explores a class of multi-network or polycontinuous geometries that share the network-like nature of the aqueous domains with the established bicontinuous cases, but not the global manifold-like smoothness of the bilayer. While the bicontinuous phases contain *two* aqueous network-like compartments, these multi-network mesophase geometries (as yet unobserved in experimental lipid systems) have three, four or more network-like aqueous domains. For example, the so-called **3etc**(187,193) structure, shown in Figs. 1 and 3, consists of three intergrown identical **etc** networks.

Even for the polycontinuous geometries studied here, the head group surface (that is, the interface separating the hydrophobic bilayer from the aqueous domains) is a smooth surface; in the remainder of this article it is modelled by a constant mean curvature (CMC) surface¹⁹, as is commonly assumed for cubic bicontinuous lipid systems²⁰.

However, in contrast to the manifold-like head-group surface, the bilayer

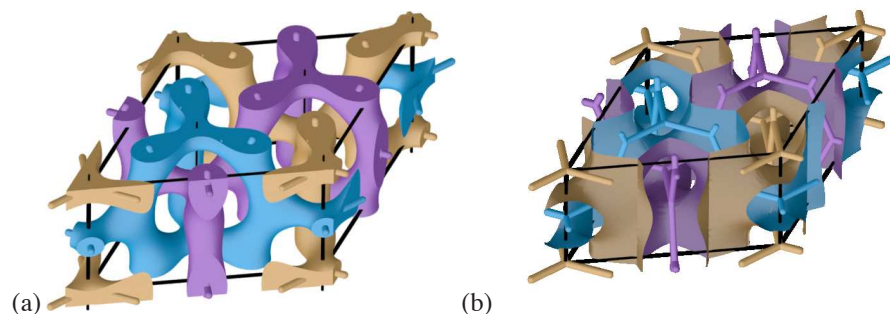


Fig. 3 The **3etc**(187,193) geometry of hexagonal symmetry with three intertwined aqueous domains. The aqueous domains are bounded by CMC surfaces and the mid-surface of the bilayer has (vertical) branch lines along which three patches meet (right). For clarity, the CMC surfaces bounding the three aqueous domains are displayed with different colours; in the mesophases described here the aqueous domains are indistinguishable. This geometry (with $a = 8.84$ nm and $c = 8.43$ nm) has been asserted as the spatial structure of the IBN-9 mesoporous silicate¹⁸.

mid-surface (which does not represent a physical interface) cannot be a smooth surface everywhere but rather must have *triple lines* along which three patches meet; these triple lines necessarily arise from the fact that the surface separates three or more network-like domains; in the bicontinuous cubic phases, the bilayer mid-surface is a globally manifold-like smooth surface, in fact it is generally treated as the triply-periodic minimal surface itself. In the multi-network phases, the bilayer mid-surface can be modelled as a branched minimal surface, consisting of smooth minimal surface patches (locally corresponding to interfaces between two of the aqueous domains) with three of them meeting along triple-lines (corresponding to points in the bilayer that are equidistant to three aqueous domains). For the case of tetracontinuous structures four triple-lines can meet at vertices equidistant to all four domains.

Figure 1(c) shows the branched bilayer mid-surface of the **3etc**(187,193) mesophase geometry; in that case, the triple-lines are straight lines along the crystallographic c -axis coincident with some of the three-fold symmetry axes. Figure 4 shows a different example of a three-network structure, called **3dia**(24,220) and composed of three interthreaded Diamond networks (the same as the net of the Q_{II}^D phase, only slightly distorted since one dimension is compressed by a factor of $\sqrt{2}$). The triple-lines in this case are arranged in the Γ -rod packing²⁴ of symmetry $I4_132$.

These branched surfaces have been termed *multi-* or *polycontinuous*^{25–28}, in analogy to the term *bicontinuous* for surfaces that divide space into two network-like compartments. More specifically, the term *tricontinuous* is used for a system with three interpenetrating nets and *tetracontinuous* for a surface that separates four interpenetrating nets.

Here we refer to the different surface geometries by names that contain the number of interthreaded nets and the name of the net; in parentheses, we provide first the coloured symmetry group of the structure (applicable if all nets are distinct) and second the uncoloured symmetry group of the structure (applicable if

	Coloured	a, b, c	Uncoloured	a, b, c	RCSR
4srs (24,208)	$I2_12_12_1$ no. 24 orthorhombic	$a = b = c$	$P4_232$ no. 208 cubic		srs-c4
4srs (5,133)	$C2$ Nr.5 monoclinic	$a = b = c$ $\beta = 90^\circ$	$P4_2/nbc$ no. 133 tetragonal	$\frac{c}{a} = \frac{1}{\sqrt{2}}$	srs-c4*
3etc (187,193)	$P\bar{6}m2$ no. 187 hexagonal	$\frac{c}{a} = \frac{0.954}{\sqrt{3}}$	$P6_3/mcm$ no. 193 hexagonal	$\frac{c}{a} = 0.954$	etc-c3
3dia (24,220)	$I2_12_12_1$ no. 24 orthorhombic	$a = b = c = 1$	$I\bar{4}3d$ no. 220 cubic		dia-c3
2srs (214,230) Q_{II}^G	$I4_132$ no. 214 cubic		$Ia\bar{3}d$ no. 230 cubic		srs-c2
2dia (227,224) Q_{II}^D	$Fd\bar{3}m$ no. 227 cubic		$Pn\bar{3}m$ no. 224 cubic		dia-c2
2pcu (221,229) Q_{II}^P	$Pm\bar{3}m$ no. 221 cubic		$Im\bar{3}m$ no. 229 cubic		pcu-c2

Table 1 Naming convention of polycontinuous geometries. “Coloured” is the symmetry group of the structure if the different network domains are of different colour or if they are chemically distinct. (Note that the symmetry group $C2$ of the achiral **4srs**(5,133) structure is the same as $I2_1$.) “Uncoloured” is the symmetry group of the structure if the network domains are identical (in colour, chemical composition, etc) – this latter is hence the space group relevant for the self-assembly described in this article where the networks represent identical aqueous domains. Space group numbers refer to the International Tables of Crystallography²¹, and RCSR to the name of this structure in the *Reticular Chemistry Structure Resource* database^{22,23}. Symmetries of the cubic geometries **2srs**(214,230), **2dia**(227,224) and **2pcu**(221,229) underlying the inverse bicontinuous Q_{II}^G , Q_{II}^D and Q_{II}^P phases are provided for reference.

the interthreaded nets are identical, as is the case for the mesophases proposed in this article). Symmetry groups are specified by their numbers as listed in ref.²¹. This scheme is similar to the names used in ref.²⁹, with the addition of the uncoloured symmetry group. Table 1 summarises the names and symmetries of the polycontinuous structures studied here.

Even from a purely geometric perspective, our understanding of polycontinuous surfaces is still in its infancy. An early example of a tricontinuous surface was Elser’s cubic archimedean screw³⁰, a branched surface separating three channels each of which is represented by the **srs** net (the same net as in the Q_{II}^G -Gyroid phase); other examples were proposed by Schoen (“integral varifolds”⁸) and by Hyde and co-workers^{25–28}. If a branched *minimal* surface is the result of area minimisation it satisfies Plateau’s laws (facets meet at 120° angles along triple-lines, and triple-lines meet at tetrahedral angles at four-fold vertices) and can be

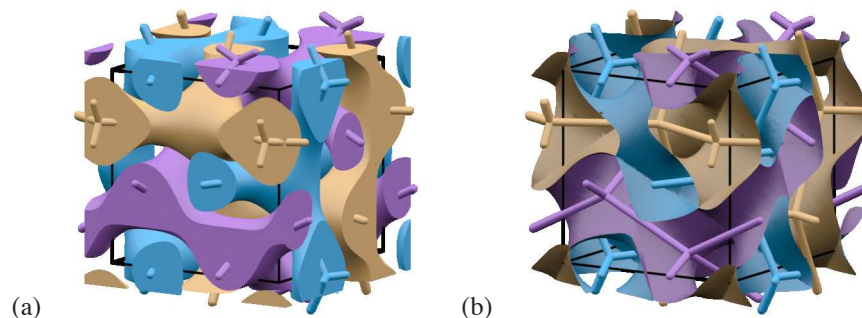


Fig. 4 The $3\text{dia}(24,220)$ geometry consisting of three distorted Diamond distorted (**dia**) nets. For clarity, the CMC surfaces bounding the three aqueous domains are displayed with different colours; in the mesophases described here the aqueous domains are indistinguishable.

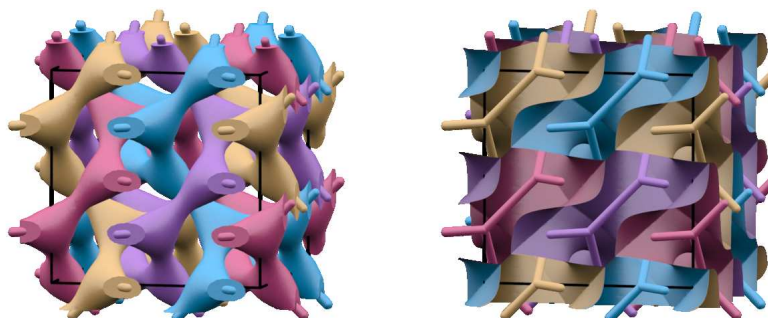


Fig. 5 The chiral $4\text{srs}^*(24,208)$ geometry consisting of four same-handed **srs** networks (the same network as that of the well-known Q^G Gyroid phase). For clarity, the CMC surfaces bounding the four aqueous domains are displayed with different colours; in the mesophases described here the aqueous domains are indistinguishable.

interpreted as dry liquid foams with infinite cells^{27,30}. (Note that below we do *not* derive the branched surfaces from an area minimisation principle, but rather as the centred mid-plane between network domains bounded by CMC surfaces, in contrast to the construction of ref²⁹. If these two different constructions lead to the same branched surface (and if so, for which values of h_0) is an interesting question for future research.

Both topologically and geometrically, many aspects of polycontinuous surfaces are closely related to the intergrowth of periodic networks. Just as the bicontinuous Gyroid is the interface between two intergrown **srs** nets, all polycontinuous surfaces can be interpreted as the dividing interface between multiple intergrown periodic nets. The intergrowth of nets was addressed (albeit not comprehensively) by Wells³¹ who was, for example, aware of the possibility to interthread four (equal-handed) **srs** nets while maintaining cubic symmetry giving the $4\text{srs}^*(24,208)$ structure shown in Fig. 5; a number of multiply intergrown nets (that are of relevance for metal organic frameworks) are described in the *Reticular Chemistry Structure Resource* database^{22,23}. A promising systematic approach for the enumeration of multiply-intergrown nets of arbitrary complex-

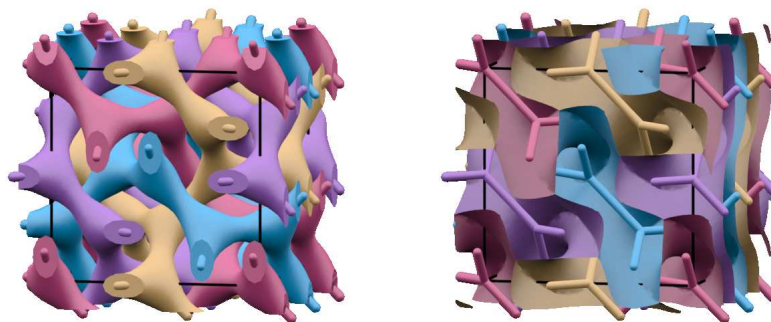


Fig. 6 The achiral $4srs(5,133)$ geometry consisting of four srs networks (the same network as that of the well-known Q^G Gyroid phase), two right-handed and two left-handed. For clarity, the CMC surfaces bounding the four aqueous domains are displayed with different colours; in the mesophases described here the aqueous domains are indistinguishable.

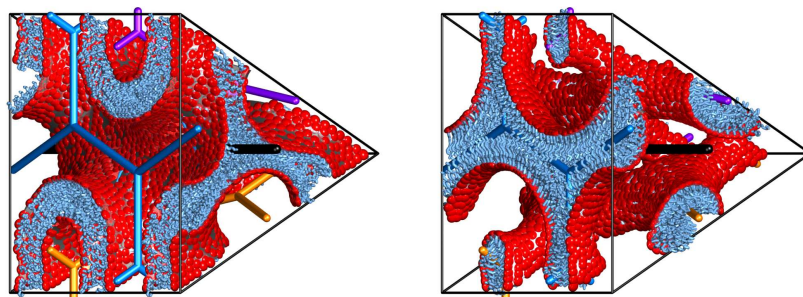
ity is the projection of forests (packings of unconnected trees) in the hyperbolic plane onto triply-periodic minimal surfaces^{26,32,33}.

Experimental or simulated realisations of polycontinuous geometries are being explored in a few distinct systems with important differences: Hyde *et al.* have proposed tricontinuous surfaces as a natural candidate for the self-assembly of star-shaped molecules with three mutually immiscible arms in a radial arrangement²⁹, such as *mikto-arm star copolymers*^{34–36} and *star polyphiles*³⁷. By microphase separation, the three immiscible components self-assemble into three distinct nanodomains; the molecular centres of such molecules are located on the branch lines where these three domains meet (the triple lines discussed above); the interface between these domains can be regarded as a branched surface. Many different structures formed by such tri-arm stars have been reported based on experiments^{34,36,38} and simulations^{39,40}. However, to date there are only hints towards the existence of tricontinuous structures, in which each of the domains forms a single connected network^{34,41}.

Importantly, in these instances, the existence of three distinct compartments or domains directly reflects the molecular architecture with three immiscible parts. While the three domains may be geometrically the same, each of them represents a chemically distinct molecular component. This is in contrast to the hypothetical systems proposed in this article where all aqueous domains are identical and the lipid molecules are amphiphilic, with only *two* (and not three) immiscible moieties, one polar and one hydrophobic.

A tricontinuous $Im\bar{3}m$ thermotropic liquid crystal phase has also been reported, based on three intergrown networks⁴²; this phase is more closely related to the structures proposed in this article in that the constituent molecules consist of two immiscible parts only; the hydrocarbon tails fill the matrix between three networks (two of which are identical) formed by the aromatic domains. The unlike network is intergrown between the two identical networks, such that the surface between these is not branched. Therefore, this structure is not tricontinuous in the strict sense of our terminology²⁹;

The experimental realisation of a tricontinuous system that is most closely



(a) type II (inverse)

(b) type I (direct)

Fig. 7 Inverse (type II) and direct (type I) conceptions of the **3etc**(187,193) structure. In inverse phases –which are the focus of this article– the network domains are water-filled and the matrix domain in between the water channels is occupied by the lipids. In direct phases (type I) the network domains are hydrophobic representing the lipid tails and the intermediate space is water.

related to the predictions of this article is the tricontinuous mesoporous silicate structure IBN-9 with hexagonal symmetry reported by Han *et al.*^{18,43–45}. This solid structure has been reported to consist of three hollow channels following the three nets of the **3etc**(187,193) structure, see Fig. 3, with a solid “matrix” of amorphous silicate as the branched sheet separating these channels and with unit cell size $\approx 8.5\text{nm}$. IBN-9 was synthesised according to methods developed for mesoporous silicates under alkaline conditions, that is, self-assembly of surfactant molecules in an aqueous solution (of ammonia) in the presence of tetraethoxysilane (TEOS) as a silica source, heated to 50°C for 24h, then calcined at 550°C .⁴³ While the earliest work⁴³ used a custom-designed cationic surfactant (denoted S2–C14), the structure has now been replicated with the more conventional surfactant CTAB⁴⁴.

With the noteworthy exception of the tricontinuous mesoporous material IBN-9, all mesoporous inorganic phases formed in the presence of amphiphilic molecules adopt mesostructures that are identical to known liquid crystalline mesophases. It is likely that the new tricontinuous material also has a liquid crystalline counterpart with the same mesostructures, though no example has been reported to date. If extant, it is an open question if IBN-9’s liquid crystalline counterpart is a direct (type I) or inverse (type II) phase, see Fig. 7. For two other mesoporous silicate geometries^{46,47}, MCM-48 (with an amorphous silica sheet draped onto the Gyroid TPMS⁴⁸) and MCM-41 (cylindrical hollow tubes in amorphous silica), it has been reported⁴⁹ that the silica “fills” the aqueous domains; MCM-48 is templated from a type-I (or direct) surfactant phase Q_I^G with hydrophobic network domains separated by a water-filled matrix (as observed in a similar surfactant system⁵⁰). In analogy, one may expect IBN-9 to be templated from a type-I **3etc**(187,193) phase. If this is indeed the case, the analysis below –for the likelihood of formation of inverse (type II) polycontinuous cases– is only of indirect relevance to the formation of IBN-9.

Much of the phase behaviour and many of the adopted spatial structures can be rationalised by purely geometric considerations⁵¹, in particular the phase se-

quence observed with changes in experimental parameters. In a nutshell, one reduces the self-assembly process to a geometric packing problem of identical particles. The particle shape is largely quantified by the *surfactant packing parameter* $s' = v_m / (a_m l_m)$ where a_m is the effective head group area, v_m the volume and l_m the length of the (fluctuating) lipid tail^{51–55}, with an implicit assumption that particles are monodisperse in volume (or size). The actual chemical parameters such as salt concentration, temperature, etc. tune the molecular shape which is the effective variable that determines the resulting self-assembled spatial structure. For example, increased salt concentration leads to a reduction of the effective head group area, as repulsive electrostatic interactions between the polar head groups are more strongly screened.

Through a theorem known as Steiner's theorem (that states that the volume in normal direction from a surface patch up to a distance l is a polynomial in l with the surface curvatures as the coefficients), the surfactant shape parameter relates to surface curvatures, see also eq. 5, and hence to the wide field of Helfrich functionals and preferred curvature energies^{15,51,56}.

The idea underlying the calculation of free energies of the self-assembly process is simple: how favourable a spatial structure is for the self-assembly of lipids of a given shape depends on how similar the space available to each molecule is to the shape of the molecule itself. This principle is elucidated by the following construction: For a given spatial configuration of lipid molecules –equilibrium or not– the hydrophobic domain is tessellated into small volumes elements (“volumes”) each of which corresponds to the region of space associated with a particular lipid molecule; this could be achieved e.g. by a Voronoi construction. The self-assembly process then favours spatial structures with minimal deviations of the shape of the molecule from the shape of the volume available to that molecule. Two factors contribute to this:

First, the *average* shape of all volume elements should match the molecular shape. This leads to the conclusion that molecules with $s' = 1$ should form flat lamellar structures, with $s' = 1/3$ spherical micelles, with $s' = 1/2$ cylindrical columns, and those with $s' > 1$ inverse structures.

Second, variations of the shape of the volume elements at different points in the adopted spatial structure are possible; while for a direct micellar or columnar (with lipids pointing inwards) the shape of the volume elements is the same at all points, variations occur for inverse micellar and columnar phases and for both direct and inverse bicontinuous phases. Therefore, even though the average shape of the volume elements may match the molecular shape, the agreement between molecular shape and shape of the volume elements varies from molecule to molecule. This phenomenon has become known as frustration or (lack of) homogeneity, with bending frustration denoting the variations of curvature throughout the structure and stretching frustration denoting the variations in the length of the volume elements (or bilayer half-width)^{11,12,14,16,17,20,54,57–60}.

This geometric approach of preferred shape is explored in this article, with respect to the formation of inverse polycontinuous mesophases with more than two network-like aqueous compartments. Specifically with respect to packing and chain stretching, it is easy to leap to the suspicion that the branched nature of the lipid bilayer introduces a large degree of chain stretching and effectively

prevents these phases from forming. However, this brings up the analogy of the inverse cubic micellar phase Q_{II}^{227} which was long thought not to exist because of chain stretching, but is now part of the standard phase diagram of lipid self-assembly^{10,61}.

In this article, we analyse hypothetical polycontinuous geometries as candidate structures for lipid self-assembly under the following assumptions: The self-assembled system consists of three or four identical network-like aqueous domains, termed \bar{K} , centred on periodic intertwined (or interthreaded) networks. The aqueous domains are bounded by surfaces S of constant mean curvature (CMC) with the same topology and symmetry as the underlying network; h_0 denotes the value of the mean curvature. The aqueous domains are separated by a hydrophobic matrix K (the complement $\mathbb{E}^3 \setminus \bar{K}$ of \bar{K}) representing the branched lipid bilayer, with lipid head-groups sitting on the surface S and lipid tails pointing into the matrix domain.

We analyse the **3etc**(187,193) geometry of hexagonal $P6_3/mcm$ (cf. Fig. 3), the chiral **4srs***(24,208) geometry of cubic $P4_232$ symmetry (cf. Fig. 5) consisting of four same-handed **srs** nets, the achiral **4srs**(5,133) geometry of four intertwined **srs**, two right-handed and two left-handed, of tetragonal symmetry $P4_2/nbc$ with $c/a = 1/\sqrt{2}$ (cf. Fig.6), and the **3dia**(24,220) geometry of three distorted Diamond networks of cubic symmetry $I\bar{4}3d$ (cf. Fig. 4).

Table 1 summarises the symmetry groups of these polycontinuous geometries (coloured and uncoloured groups) and Table 2 provides maximal bilayer volume fractions for these polycontinuous geometries.

2 Structural homogeneity and surfactant shape parameter

The conclusions of this article are based on an analysis of structural homogeneity, quantified by the degree of variation of both local bilayer width and local shape variation. We identify the spatially-varying half-width $d(p)$ of the (branched) bilayer at points p on S as well as the local volume element $dK(p)$ that represents the section, or “volume element”, of the bilayer that is associated with a small surface patch $dS(p)$ at point p on the head-group surface S ; $dS(p)$ can be considered to represent a single molecular head-group, see Fig. 8.

The construction of both the local volume elements $dK(p)$ and the measurement of the bilayer half-width $d(p)$ is conceptually simple, see Fig. 8, drawing on the medial surface (or axis) construction^{13,14,60,62,63} (see also refs.^{64,65}). Consider the body K that represents the branched lipid bilayer and that is bounded by the CMC interfacial surfaces. The *medial surface* $MS(K)$ is the centred mid-surface (sometimes called backbone) of K with the defining feature that any point q on the medial surface is equidistant to (at least) *two* closest points p_1 and p_2 on the bounding surface S . For all of the multiply interthreaded CMC network structures considered here, the definition of the MS can be further simplified. For these structures, the bounding surface S of K evidently consists of separate CMC surfaces S_i with $i = 1, 2, 3$ (tricontinuous) or $i = 1, 2, 3, 4$ (tetracontinuous) corresponding to the three or four network-like aqueous domains. In these cases, the points p_1 and p_2 are always on two *different* surfaces S_i (bounding different aqueous domains), i.e. $p_1 \in S_i$ and $p_2 \in S_j$ with $i \neq j$. The MS thus correctly represents the bilayer mid-surface equidistant from the different aqueous domains.

Name	Uncoloured	a, c	H_{min}	ϕ_{BL}^{min}	Fig.
Q_{II}^G	$Ia\bar{3}d$	$a = 1$	0	0	2
3etc (187,193)	$P6_3/mcm$	$a = 1, c = 0.79$	3.15 ± 0.15	0.50 ± 0.05	–
		$a = 1, c = 0.954$	3.1 ± 0.1	0.40 ± 0.05	1, 3, 7
		$a = 1, c = 1.10$	3.15 ± 0.15	0.38 ± 0.05	–
3dia (24,220)	$I\bar{4}3d$	$a = 1$	unknown	unknown	4
4srs (5,133)	$P4_2/nbc$	$a = 1/\sqrt{2}, c = 1/2$	2.5 ± 0.1	0.30 ± 0.01	6
4srs* (24,208)	$P4_232$	$a = 0.5$	2.5 ± 0.1	0.30 ± 0.01	5
Q_{II}^{227}	$Fm\bar{3}m$	$a = 1$	$1/(2\sqrt{2})$	$1 - \frac{\pi}{\sqrt{18}} \approx 0.26$	–
H_{II}	$p\bar{6}m$	$a = 1$	$1/2$	$1 - \frac{\sqrt{3}\pi}{6} \approx 0.10$	–

Table 2 Structural data for the polycontinuous space partitions. H_{min} is a rough approximation of the minimal mean curvature h_0 for which the CMC network domains are non-overlapping. ϕ_{BL}^{min} is the corresponding volume fraction of the branched lipid bilayer (matrix domain) and represents the smallest bilayer volume fraction that is possible for the respective geometries. The value of the parameter a provides the overall structural length that does not enter the results of Figures 9 to 12, but is necessary when specifying H_{min} ; c and a refer to the values of the uncoloured space groups that are relevant to lipid self-assembly with identical channels. For the **4srs**(5,133) and the **4srs***(24,208) structures, the values of H_{min} and ϕ_{BL}^{min} correspond to the mean curvature where the CMC surfaces bounding the four network domains have a contact point; the value is the same for both structures as the first contact point (that develops when decreasing h_0 below H_{min}) is a contact point between a pair of same-handed networks which are present in both structures (i.e. the branched bilayer has a point of vanishing thickness, for $h_0 = h_{min}$). The minimal bilayer half-width $d_{min}(h) = \min_{p \in S} d(p)$ is, for $h \rightarrow h_{min}$ and $h > h_{min}$, a function that smoothly decreases to $d_{min}(h_{min}) = 0$ for these **srs** geometries. For the **3etc**(187,193) structure, this is different, because of the discontinuous behaviour as a function of h_0 discussed in Fig. 17; at $h_0 = h_{min}$ the bilayer jumps from having finite width everywhere to an overlapping configuration. A configuration in which the **etc** network domains do not overlap but have singular mutual contact points (as is the case for the **4srs** and **4srs*** structures at h_{min}) does not exist.

The medial surface construction provides a concise definition of the bilayer mid-surface, in agreement with intuition for the self-assembly geometries that have been experimentally realised: For inverse hexagonal cylinder phases H_{II} , the MS represents the hexagonal honeycomb structure that separates the different cylindrical aqueous compartments, see e.g. Fig. 3 in ref.²⁰ and Fig. 8. Similarly for the $Fd\bar{3}m$ inverted micellar phases in binary systems, the MS traces the polyhedral cells between the water-filled micelles (see Fig. 9 in ref.¹⁰), and analogous for the hexagonal inverse micellar phase⁶⁶. For the inverse bicontinuous phases Q_{II}^G , Q_{II}^P and Q_{II}^D based on Schwarz' and Schoen's Gyroid, Primitive and Diamond minimal surfaces^{8,9,67}, the medial surface is very close (and possibly coincides exactly) with the minimal surface*, see Fig. 2 and Fig. 1 in ref.²⁰. For

* Note the distinct difference to the use of the medial surface construction in refs.^{13,14,60,62,63}. Here we determine the MS of the branched bilayer bounded by the CMC surfaces representing the head group interface; in this situation the MS is inside the branched bilayer and corresponds, or is at least close,

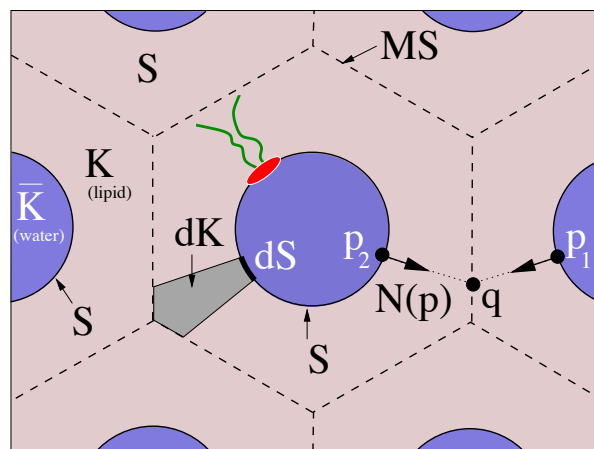


Fig. 8 Construction of the medial surface and the local volume element $dK(p)$ illustrated for a hexagonal inverted H_{II} phase. The medial surface is the centred mid-surface of the branched lipid bilayer, with each medial surface point equidistant to two (or more) points on the bounding surfaces S of two different aqueous domains. The bilayer half-width at a given interface point p on the CMC head group surface corresponds to the distance $d(p)$ from p to its image on the medial surface, see eq. (2). For a given surface patch dS on the CMC head group surface, the corresponding volume is defined as the space between dS and its image on the medial surface, see eq. (3).

the type-I hexagonal H_I , micellar Q_{II}^{227} , and lamellar L_α lipid phases the MS are simply the cylinder rotation axes, the micellar centre points and the bilayer half-plane (when approximating the head group interfacial surface by CMC surfaces, i.e. by cylinders, spheres or planes).

The MS construction immediately provides a definition of the point-wise bilayer width at point p on the head-group surface S , as the distance $d(p)$ from p to its corresponding point $ms(p)$ on the MS. As $ms(p)$ is strictly in the surface normal direction¹³, the distance $d(p)$ and the MS point $ms(p)$ can be expressed by a max-min principle: For a given point $p \in S$, the corresponding MS point $ms(p)$ is the maximally distant point in direction of the surface normal $N(p)$ from p that is still closer to p than it is to any other point $p' \in S$ with $p' \neq p$ (The surface normal $N(p)$ is assumed to point into the hydrophobic domain). Therefore, one obtains

$$ms(p) = p + d(p)N(p) \quad (1)$$

with the *medial surface distance function* $d(p)$ given by

$$d(p) = \max\{r \in \mathbb{R}^+ \mid D(p + rN(p), p) \leq D(p + rN(p), p') \quad \forall p' \in S\}, \quad (2)$$

with the Euclidean distance $D(p, p')$ between two points $p, p' \in \mathbb{E}^3$. One may consider the MS transform as moving point p along $N(p)$ to $p + rN(p)$ by

to the branched minimal surface. In refs.^{13,14,60,62,63}, the MS of the bicontinuous minimal surfaces is computed and the MS is a two-dimensional skeleton close to the nets or skeletal graphs centered in the aqueous domains.

a value $r > 0$. For small r it is evident that p is the closest surface point on S to the translated point $p + rN(p)$; however, for a finite r , a different point $p' \in S$ becomes the closest surface point to $p + rN(p)$; the value of r at which this happens defines $d(p)$ and the MS point $\text{ms}(p)$.

Below, the function $d(p)$ is used to quantify averages and variances of bilayer width. Through the relation of “chain stretching contributions” to the self-assembly free energy, this analysis allows for predictions of the likelihood of self-assembled experimental observation of these polycontinuous lipid structures. Chain stretching contributions are, however, only one part of energetic description. Of equal importance are “bending contributions” that relate to curvature inhomogeneities and –through the celebrated molecular shape parameter– to molecular shape. To analyse bending contributions, we construct a local volume that allows the analysis of a structural equivalent of the molecular shape parameter s' .

The guiding idea behind the definition of a volume element dK associated with a given surface patch dS is to associate each point in the bilayer K with its closest point on the interface surface, see Fig. 8. All those points in (the branched bilayer) K that are closer to the surface patch dS than to any other parts of the surface form the volume dK associated with dS . If the medial surface transform $\text{ms}(p)$ is known for all points p in S , the volume dK associated with a surface patch dS is easily evaluated as

$$dK = \{ p + rN(p) \mid p \in dS \text{ and } 0 \leq r \leq \text{ms}(p) \}. \quad (3)$$

This equation states that the volume dK associated with surface patch dS is given by all points between those of dS and their corresponding points on the medial surface.

In the following, we use the notation $dS(p)$ to denote that the surface patch contains point $p \in dS$ and to assume that $dS(p)$ is a small surface patch. Similarly $dV(p)$ denotes the volume element associated with $dS(p)$.

In the context of lipid self-assembly, the surface patch dS represents the patch of the interface surface that is occupied by the head group of a particular lipid molecule and the volume dK is the space occupied by the hydrophobic chains.

We hence define the *structural shape parameter* $s(p)$ as a property of the adopted or assumed spatial geometry, which –for equilibrium configurations– should relate to the similarly defined surfactant packing parameter s' which characterises the molecular shape, see above. The structural shape parameter is the dimensionless measure

$$s(p) = \frac{v(p)}{a(p) d(p)} \quad (4)$$

with $a(p)$ the surface area of the surface patch $dS(p)$, $v(p)$ the volume of the associated volume element $dK(p)$ and $d(p)$ its length as measured by the medial surface distance. (When applying eq. 4 to a large patch dS with significant variation of $d(x)$ over the points $x \in dS(p)$, the average $\bar{d}(p) = \int_{dS} d(p) dA / \int_{dS} dA$ should be used instead of $d(p)$.)

The bilayer half-width $d(p)$ and the structural shape parameter $s(p)$ are complementary w.r.t. the geometric characteristics they describe. The value $s(p)$ relates to the curvature properties of the interface, but is independent of the size

of the volume element. To see the relationship to curvature properties, consider the equation that relates surface curvatures to the volume swept by parallel surfaces to a given surface patch dS up to distance r (known as the Steiner formula in integral geometry). A parallel surface of the patch dS is the surface obtained by translation of all surface points of the patch in surface normal direction by a fixed distance r , $dS_{\parallel}(r) = \{\mathbf{x} + r\mathbf{N}(\mathbf{x}) \mid \mathbf{x} \in dS\}$. The region of space swept by parallel surfaces $dS_{\parallel}(p)$ as r is increased from 0 to r has volume $v(p, r) = ra(p) + r^2 a(p)\overline{H} + r^3 a(p)\overline{G}/3$ if $r < \min\{\kappa_1(p), \kappa_2(p)\}$ with the mean and Gauss curvature $\overline{H}(p) = \int_{dS(p)} HdA$ and $\overline{G}(p) = \int_{dS(p)} GdA$ averaged over all points of $dS(p)$ [†]. Assuming that the surface patch $dS(p)$ is so small that variations of the mean curvature H , the Gauss curvature G and the medial surface distance d over its points are negligible (that is, $\overline{H}(p) = H(p)$, $\overline{G}(p) = G(p)$ and $\overline{d}(p) = d(p)$) the Steiner formula provides a relation between the structural shape parameter and the curvature properties of the head group interface (see chapter 4 in ref.⁵¹)

$$s(p) := \frac{v(p)}{a(p)d(p)} = 1 + H(p)d(p) + \frac{G(p)}{3}[d(p)]^2 \quad (5)$$

While $d(p)$ has the dimension $[m]$ of a length, the parameter $s(p)$ is dimensionless, of unit $[1]$; $s(p)$ is hence insensitive to the linear size or volume of the volume element. This insensitivity to size is important for two reasons in the context of lipid self-assembly: First, $s(p)$ will not change with the overall length scale of the system, that is, it is independent of the lattice parameter a as a change in a only leads to a change of length scale for all volume elements. Second, $s(p)$ can adopt identical or similar values for two volume elements at different points p_1 and p_2 in the structure if the surface at p_2 is flatter (with smaller curvature values) and, simultaneously, has larger $d(p)$. In that case, the volume elements at p_1 and p_2 can be of very similar shape, and hence have similar structural shape parameter $s(p_1) \approx s(p_2)$, while having very different volumes $v(p_1) \neq v(p_2)$.

For the analysis of self-assembly structures, one is not interested in spatially resolved values of $s(p)$ or $d(p)$, but rather in average values and the degree of variation throughout the spatial structure. These are quantified by moments of the distributions of $d(p)$

$$\langle d \rangle = \frac{1}{A} \int_S d(p) dA, \quad \text{and} \quad (\Delta d)^2 := \langle [d - \langle d \rangle]^2 \rangle = \frac{1}{A} \int_S [d(p) - \langle d \rangle]^2 dA \quad (6)$$

and of $s(p)$

$$\langle s \rangle = \frac{1}{A} \int_S s(p) dA, \quad \text{and} \quad (\Delta s)^2 := \langle [s - \langle s \rangle]^2 \rangle = \frac{1}{A} \int_S [s(p) - \langle s \rangle]^2 dA \quad (7)$$

where S is assumed to be a translational unit cell of the structure and A the surface area of S .

[†] The validity of this formula for a sphere of radius R is easily verified by expanding the total volume $v(p, r) = v(r) = 4\pi/3(R+r)^3$ and noting that the mean curvature of a sphere with radius R and outwards pointing normals is the positive constant $H = 1/R > 0$; and similarly for a cylinder.

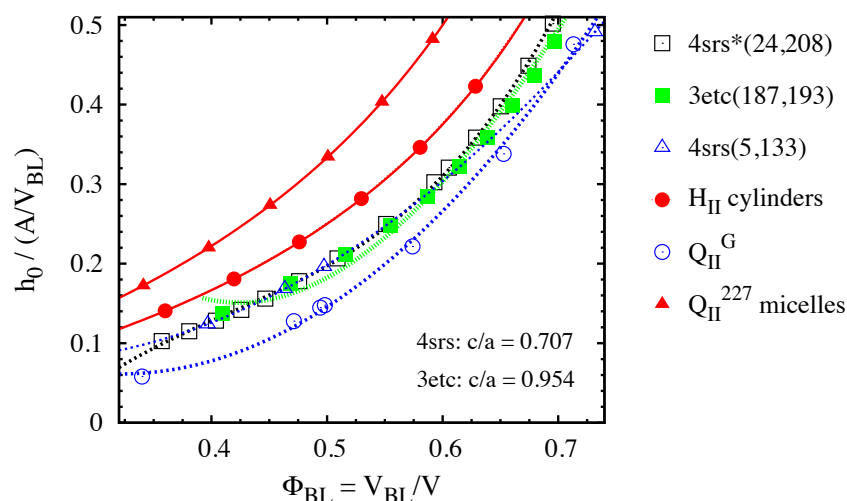


Fig. 9 Mean curvature of head group interface as function of the bilayer volume fraction ϕ_{BL} , evaluated for length scales a such that $V_{BL}/A = 1$ is constant. V_{BL} is the total volume of the bilayer (such that $V_{BL}/(V_{BL} + V_{AQ}) = \phi_{BL}$ is the bilayer volume fraction with V_{AQ} the combined volume of all aqueous domains), A the surface area of the head group interface and h_0 its (constant) mean curvature. Dashed lines are guides to the eye, solid lines the analytic curves of eqs. (22) and (9). Ratios c/a of the lattice parameters for the **etc**(187,193) and **4srs**(5,133) structures refer to the uncolored space groups.

In this article we invoke a relationship between the molecular shape described by the surfactant packing parameter $s' = v_m/(a_m d_m)$ and the structural packing parameter s : An ensemble of identical molecules best accommodates a geometric shape S whose average structural shape parameter $\langle s \rangle$ is close to the molecular packing parameter s' (global constraint) and whose variations $\langle [s - \langle s \rangle]^2 \rangle$ throughout the structure are smallest (structural homogeneity favoured by the identical shape of the constituent molecules). However, because of the size insensitivity of s it is important to equally consider a further shape descriptor that is sensitive to overall size: the bilayer half-width $d(p)$ measured by the medial surface construction is a suitable measure of the linear size of the volume elements.

This motivates the choice of $\langle s \rangle$ as a measure of the average shape of the “molecular” tiles, and $\Delta s := \sqrt{\langle s^2 \rangle - \langle s \rangle^2}$ and $\Delta d := \sqrt{\langle [d - \langle d \rangle]^2 \rangle}$ as measures of structural homogeneity. Below the geometric properties of the hypothetical multi-network geometries and the known lipid phases will be compared in terms of these measures.

3 Average molecular shape of polycontinuous lipid phases

Figures 9 and 10 shows the mean curvature $h_0/(A/V_{BL})$, normalised to constant surface-to-volume ratio, and the average structural shape parameter $\langle s \rangle$ as a function of bilayer volume fraction ϕ_{BL} . These average shape characteristics relate to the typical molecular shape that is globally (i.e. on average) commensurate with

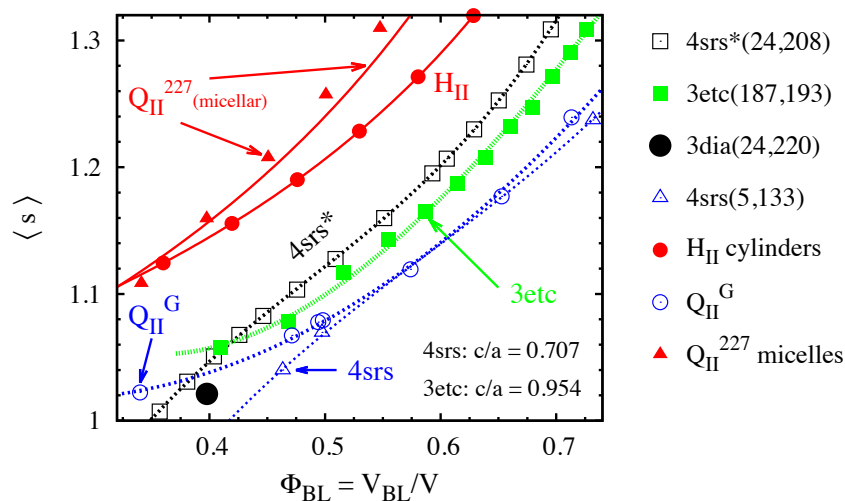


Fig. 10 Average structural shape parameter $\langle s \rangle$ indicating the molecular shape required to form the geometries. Note the small deviations between the numerical and analytical data for $\langle s \rangle$ for the inverse micellar Q_{II}^{227} phase; these deviations are due to the fact that even the average of s is a higher-order shape measure compared to the simple bilayer half-width d , as discussed in section 4. Note that for the **4srs**(5,133) and the **4srs***(24,208) geometries, the data for very low ϕ_{BL} corresponds to configurations where the CMC domains are almost in contact, see also Fig. 17. Ratios c/a of the lattice parameters for the **etc**(187,193) and **4srs**(5,133) structures refer to the uncolored space groups.

the different candidate geometries.

Data are provided as function of the bilayer volume fraction $\phi_{BL} = V_{BL}/V$ where V_{BL} is the volume of the bilayer in a given space of total volume V (which is the sum of $V = V_{BL} + V_{AQ}$ if V_{AQ} is the combined volume of all aqueous domains).

The mean curvature is analysed comparing the different candidate geometries for length scales such that the ratio of total bilayer volume V_{BL} to surface area A is 1, see Fig. 9. As the mean curvature h_0 (which for all geometries analysed in this article is a constant) decreases with increasing width of the aqueous domains, the monotonous increase of $h_0/(A/V_{BL})$ with increasing ϕ_{BL} is expected, and is observed as a common feature of all geometry types.

For a fixed bilayer volume fraction ϕ_{BL} , chosen in the interval $[0.3, 0.65]$ relevant for lipid self-assembly, Figure 9 shows that the normalised mean curvature is lowest for the bicontinuous Q_{II}^G phase, highest for the inverse micellar Q_{II}^{227} phase and with the columnar phase H_{II} taking intermediate values, in line with expectation⁶⁸. The polycontinuous cases are all intermediate to the bicontinuous cases and the columnar cylinders and, within the accuracy of our numerical analysis, all have the same value of the normalised mean curvature (with the exception of the achiral **4srs**(5,133) structure at high values of ϕ_{BL}).

Figure 10 shows the average structural shape parameter $\langle s \rangle$ (see eq. 7) as a function of bilayer volume fraction. $\langle s \rangle$ characterises the average shape, but in

contrast to the normalised mean curvature it incorporates the bilayer width. At fixed ϕ_{BL} , $\langle s \rangle$ is smaller for the inverse bicontinuous Gyroid Q_{II}^G phase and largest for the inverse micellar phase with the columnar hexagonal phase again at intermediate values, in line with previous analysis (see e.g. Fig. 4.11 in⁵¹). The values for the polycontinuous cases now differ for the different structures. For lipid volume fractions above 40% –presumably of most relevant to lipid self-assembly– the **3etc**(187,193) and the chiral **4srs***(24,208) structures are again intermediate to the bicontinuous Q_{II}^G and the inverse cylinders H_{II} . Interestingly, some polycontinuous structures (**3etc**(187,193) with $\phi_{BL} < 0.4$, the single instance of the **3dia**(24,220) structure analysed here with $\phi_{BL} \approx 0.4$ and the achiral **4srs**(5,133) structure) can have smaller values of $\langle s \rangle$ than the bicontinuous Gyroid case. All geometries show a monotonous increase of $\langle s \rangle$ with increasing lipid bilayer volume fraction ϕ_{BL} .

The conclusion to be drawn from Figures 9 and 10 is that *at least in terms of the average molecular shape* the polycontinuous phases, in particular **3etc**(187,193) and **4srs***(24,208), should be commensurate with existing molecular shapes, because their average shape measured by $\langle s \rangle$ and $h_0/(A/V_{BL})$ is intermediate to two cases (H_{II} and Q_{II}^G) that are experimentally realised.

4 Homogeneity and Packing frustration

The second determinant of phase formation, in addition to the commensurability of the molecular shape and the average geometric properties discussed above, is the structural homogeneity and its implications for bending and stretching frustration. Assuming that the average geometry matches the molecular shape, the variations throughout the structure will determine the degree of frustration – necessarily present for *all* inverse mesophase structures including cylinders and micelles. We here discuss homogeneity and packing frustration for the polycontinuous structures, by an analysis of variances of the bilayer half-width d and of the structural packing parameter s . Figures 11 and 12 show the relative variances of s and d , as defined in eqs. (6) and (7).

Figure 11 shows variations Δd of the bilayer half-width $d(p)$, measured by the medial surface distance from the head group interface to the bilayer mid-surface. As the bilayer width is a quantity of dimension [m], it is here shown relative to the average $\langle d \rangle$. Expectantly, the variations of the bilayer width are minimal for the bicontinuous Gyroid geometry where the bilayer is a smooth unbranched sheet; the small degree of variation is a signature of the modelling of the head group surface as a CMC surface rather than a parallel surface to the TPMS; for the bicontinuous Gyroid, these variations are approximately independent of the bilayer volume fraction ϕ_{BL} . The variations for the inverse cylindrical H_{II} phase are smaller than those of the FCC inverse micellar Q_{II}^{227} phase; for both geometries, the relative variations $\Delta d/\langle d \rangle$ become smaller with larger bilayer volume fraction.

The values of $\Delta d/\langle d \rangle$ for the polycontinuous cases, are, for all ϕ_{BL} , larger than those of the columnar H_{II} and the bicontinuous Q_{II}^G phase. The width variations of the chiral **4srs***(24,208) structure are, for all ϕ_{BL} slightly above those of the micellar phase. The achiral **4srs**(5,133) structure is intermediate to H_{II} and Q_{II}^{227} . The **3etc**(187,193) structure (with the same $c/a = 0.954$ as the IBN-9

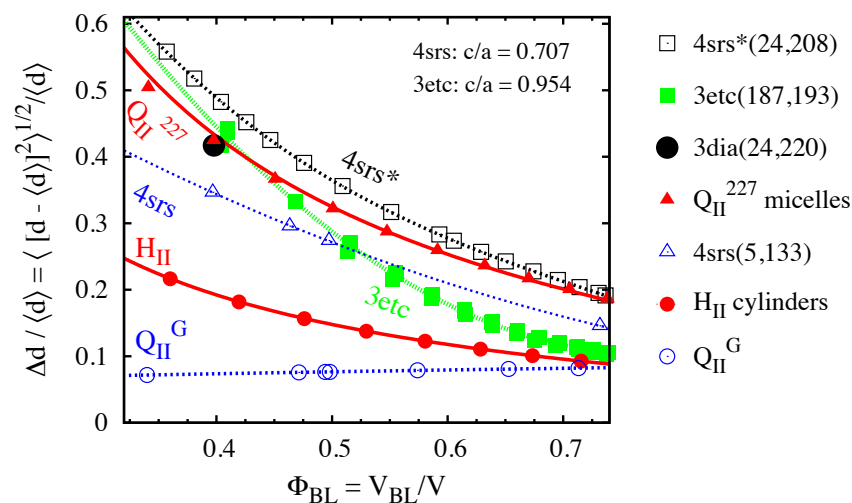


Fig. 11 Relative spatial variations $\Delta d/\langle d \rangle$ of lipid bilayer half-width d throughout the bilayer. Solid (red) straight lines are the analytic solutions of eqs. (14) and (33); dashed lines are guides to the eye only. Ratios c/a of the lattice parameters for the **etc**(187,193) and **4srs**(5,133) structures refer to the uncolored space groups.

phase) has large variations $\Delta d/\langle d \rangle$ for low ϕ_{BL} similar to the inverse micellar phase that however decrease more rapidly with increasing ϕ_{BL} than for the other geometries; for large $\phi_{BL} \approx 70\%$, the variations are comparable to the H_{II} and the bicontinuous Gyroid geometry.

In terms of bilayer width variations, the inverse polycontinuous geometries are hence fairly inhomogeneous compared to the inverse bicontinuous Gyroid phase. Nevertheless, their spatial homogeneity with respect to d is similar or smaller than the inverse micellar phase. Similar to the inverse micellar phase, that (despite its high degree of packing frustration^{10,69}) has by now been found in a number of systems including purely binary ones⁶¹, one would probably expect the polycontinuous examples to form for large bilayer volume fractions ϕ_{BL} , i.e. for molecules with long chains relative to their head group area and small head group area or low water content.

In terms of the structural shape parameter s , Fig. 12 clearly demonstrates that both the inverse bicontinuous and the inverse polycontinuous structures are far more heterogeneous than the inverse hexagonal H_{II} or the inverse micellar Q_{II}^{227} phase, with larger values of Δs . While Δs of the polycontinuous **4srs**(5,133), **3etc**(187,193) and **3dia**(24,220) is significantly larger than for the bicontinuous Q_{II}^G phase, the value for the cubic and chiral **4srs***(24,208) is very similar to that of the bicontinuous Q_{II}^G Gyroid phase, for a large range of bilayer volume fractions, in particular around $\phi_{BL} \approx 40\%$.

The structural shape parameter $s(p)$ is a more complex shape measure than the simple bilayer (half-)width $d(p)$. It combines aspects of the surface curvatures $H(p)$ and $G(p)$ with $d(p)$, see eq. (5). If the curvature properties are constant (as is the case for the approximation of H_{II} and Q_{II}^{227} where the head

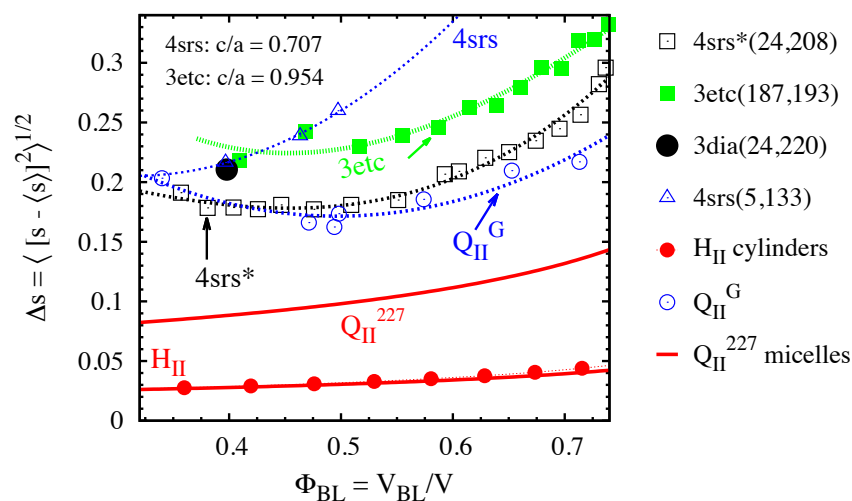


Fig. 12 Relative spatial variations Δs of structural shape parameter s throughout the bilayer. For the inverse micellar data, we only show the analytic solution given by eq. (35) and not computational data that deviates significantly (by a factor of approximately 2) from the analytic curve. The origin of this deviation is the difficulty of measuring Δg which incorporates fourth moments $\langle d^4 \rangle$ of the distribution of bilayer width. This provides a caution for the accuracy of the data for other geometries. However, we have verified that the results presented are consistent when representing the geometries by triangulations of different resolution. Ratios c/a of the lattice parameters for the **etc**(187,193) and **4srs**(5,133) structures refer to the uncolored space groups.

group surface is modelled as cylinders and spheres) averages and variances of the s and d are closely related. For the hexagonal cylinders with constant mean curvature $H(p) = H \neq 0$ and vanishing Gauss curvature $G(p) = 0$ for all points on the cylinder head group surface, eq. (5) immediately yields $\langle s \rangle = 1 - H \langle d \rangle$, $\langle s^2 \rangle = 1 - H \langle d \rangle + H^2 \langle d^2 \rangle$ and $(\Delta s)^2 = (\langle d^2 \rangle - \langle d \rangle^2) \times H^2$. This identity is evidently also seen in eqs. (12), (14), (18) and (20) for the analytic expressions for Δd and Δs . For the inverse micelles, where the Gauss and mean curvatures $G(p) = G = 1/R^2$ and $H(p) = H = 1/R$ are spatially constant (R is the cylinder or sphere radius), combining eqs. (5), (6) and (7) yields expressions for the average and variance of s explicitly as a function of the moments of d : $\langle s \rangle = 1 + H \langle d \rangle + G/3 \langle d^2 \rangle$ and $\langle s^2 \rangle = 1 + 2H \langle d \rangle + (H^2 + 2G/3) \langle d^2 \rangle + 2HG \langle d^3 \rangle + G^2/6 \langle d^4 \rangle$. (The appearance of higher moments of d in this formula for $\langle s^2 \rangle$ is consistent with the noise sensitivities of the numerical computations, see caption of Fig. 12). For surfaces with variations of curvatures –including all bicontinuous and polycontinuous surfaces– the moments of s are not only a function of the moments of d , but include moments of the distributions of Gauss curvatures G and, unless $H = \text{const}$, of H .

Importantly, s and its averages and higher moments are dimensionless and scale-invariant. Hence Δs is not sensitive to spatial variations of the size of the local volume elements, in contrast to $\Delta d / \langle d \rangle$. Assuming the molecules to be

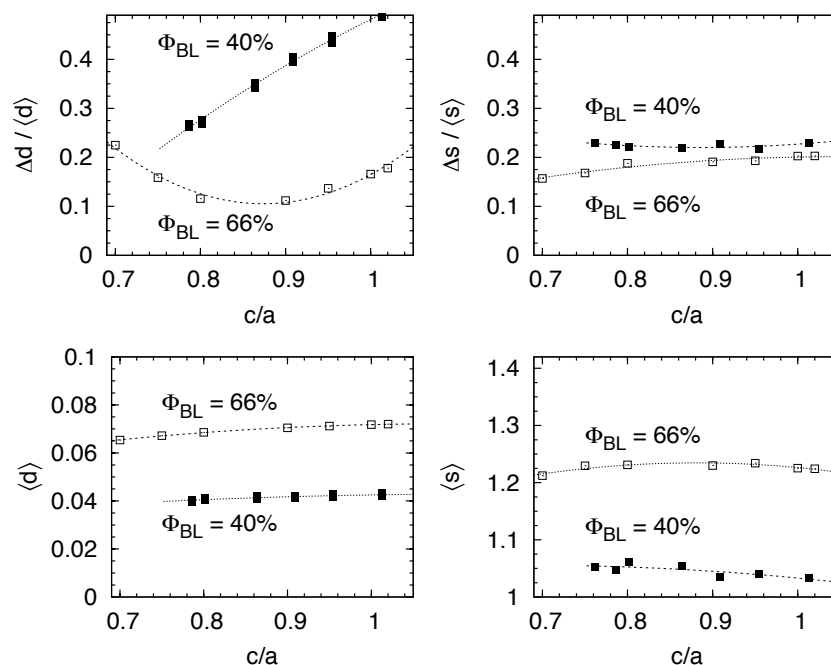


Fig. 13 Homogeneity and average shape of the tricontinuous $3etc(187,193)$ structure as function of the crystallographic c/a ratio (in the uncolored symmetry group $P6_3/mcm$); the bilayer volume fraction of 40% is close to that observed in the experimental mesoporous IBN-9 phase which has $c/a = 8.84/8.43 \approx 0.95$. The minimum of the parabola fitted to the data for $\Delta d / \langle d \rangle$ for $\phi_{BL} = 66\%$ is at ≈ 0.87 . The average bilayer half-width $\langle d \rangle$ of dimension [m] is for a system with $a = 1$. Polynomials of degree two are fitted to the data as guide to the eyes.

largely incompressible, a volume constraint appears to be required. In that sense, it seems likely that variations in size of the local volume elements, partially covered by Δd , may be a primary requirement, with variations of s a second-order effect to favour equal shape amongst the elements with equal volume.

For the structures with cubic symmetry, i.e. $4srs^*(24,208)$ and $3dia(24,220)$, the sole free parameter is the lipid volume fraction ϕ_{BL} . The overall length scale, given by the lattice parameter a , does not affect the data in the form presented here. For the tetragonal $4srs(5,133)$ and the hexagonal $3etc(187,193)$ structure, the crystallographic c/a -ratio is a further free parameter that needs exploration when searching for the optimal structure.

Figure 13 shows data for average shape and spatial homogeneity for the $3etc(187,193)$ structure as function of the hexagonal c/a ratio, for two different bilayer volume fractions. The key observation is that, for both $\phi_{BL} \approx 40\%$ and $\phi_{BL} \approx 66\%$, the average shape is largely independent of the c/a -ratio, both in terms of $\langle d \rangle$ and $\langle s \rangle$. Further, it also appears that variations of the shape of $dK(p)$ quantified by $\Delta s / \langle s \rangle$ are largely constant. However, the variations in relative bilayer (half-)width $\Delta d / \langle d \rangle$ change significantly with c/a . At $\phi_{BL} \approx 40\%$ the variations clearly favour smaller c/a ratios. At $\phi_{BL} \approx 66\%$, the situation is different

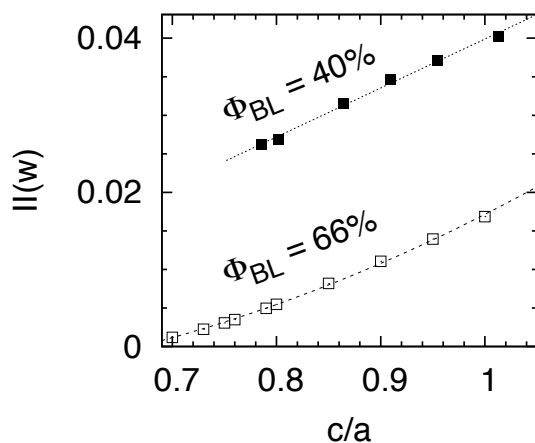


Fig. 14 Anisotropy of the surface orientation of the **3etc**(187,193) geometry as function of the c/a ratio (in the uncolored symmetry group $P6_3/mcm$), for $\phi_{BL} \approx 66\%$ and $\phi_{BL} \approx 40\%$. $II(w) = \text{tr}(w^2)/2$ is the second invariant of the interface tensor $w_{ij} = (1/A) \int_S (n_i n_j - \delta_{ij}/3) dA$ where A is the surface area of S and n_i the i -th component of the surface normal^{63,70}. A value $II(w) = 0$ indicates isotropy, and values > 0 deviations from isotropy. The measure $II(w)$ is the same as analysed in ref.⁶³; however, when comparing absolute values, note that the values for $II(w)$ shown in Fig. 3 (top) of ref.⁶³ are incorrect and too large by a constant factor of 10.

and $\Delta d/\langle d \rangle$ has a most homogeneous member with c/a ratio of approximately 0.87. Given that all other relevant measures appear to be almost independent of c/a , one would expect a lipid inverse **3etc**(187,193) phase to have lattice ratios $c/a \approx 0.87$ (w.r.t. the uncolored space group $P6_3/mcm$).

It is interesting to note that $c/a = 0.87$ is only approximately 10% smaller than the c/a ratio of the mesoporous IBN-9 silicate, $c/a = 84.3/88.4 \approx 0.95$. This agreement would be a strong indication of the relevance of our homogeneity analysis for the self-assembly of polycontinuous phases if two conditions were met: (a) the lipid precursor phase of IBN-9 is indeed an inverse phase (which is not likely to be the case, see section 1); and (b) that the lipid volume fraction of this precursor phase was significantly higher ($\approx 66\%$) than the solid volume fraction of the resulting IBN-9 (which is $\approx 40\%$ ⁴³). While this is unlikely to be the case, this result still provides an expectation value for c/a for a hypothetical inverse **3etc**(187,193) phase.

In ref.⁶³ the observation was made that the most homogeneous member of a (to-date hypothetical) bicontinuous hexagonal mesophase based on Schwarz H surface is isotropic in terms of (a) the Doi-Ohta interface tensor, and (b) in terms of the elastic moduli of a bilayer sheet that was assumed to be homogeneous and linear-elastic⁶³. This has inspired the analogous analysis, of structural isotropy of the **3etc**(187,193) structure, see Fig. 14. In contrast to the hypothetical bicontinuous H mesophase of ref.⁶³, no correlation between the most homogeneous member for the $\phi_{BL} \approx 40\%$ structures at $c/a \approx 0.87$ and structural isotropy was found. Further, treating the branched linear bilayer of the **3etc**(187,193) struc-

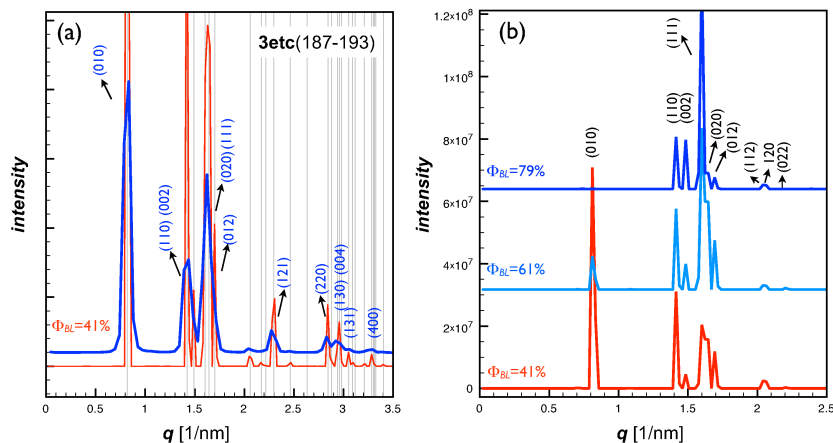


Fig. 15 (a) Simulated scattering pattern of the **3etc**(187,193) structure close to the experimentally observed conditions⁴³: The lattice parameters are $a = 8.84\text{nm}$, $c = 8.43\text{nm}$, and the aqueous channel domains take up a volume of 59% (i.e. $\phi_{BL} = 41\%$). The red curve demonstrates data for the ideal, strictly periodic model at high spatial resolution, and the blue curve a simulation of lower resolution. The grey lines depict all allowed hkl values. (b) Simulated SAXS patterns for different volume fractions ϕ_{BL} of the lipids. Interestingly, the intensity of the (010) peak or the ratio between the (110) and (002) reflection are so sensitive to ϕ_{BL} that they may well serve as an independent measure for ϕ_{BL} .

ture as a homogeneous linear-elastic sheet (by the same method used as in ref.⁶³ using the finite element methods of ref.^{71–73}), the structures showed, for all c/a , an elastic tensor with a clear signature of hexagonal symmetry that, in contrast to Schwarz' Hexagonal surface⁶³, does not exhibit any unexpected degeneracies of the eigenvalues of the Mehrabadi matrix.

5 Simulated SAXS patterns

Small angle X-ray scattering is by far the most common experimental method for structure assignment of self-assembled lipid-containing phases. We therefore provide SAXS powder scattering patterns (azimuthal-averaged radial scattering intensities) for the hypothetical tetracontinuous **4srs**(5,133) and **4srs***(24,208) structures and the tricontinuous **3dia**(24,220) structure. Interestingly, for the latter two cases, the scattering patterns bear remarkable resemblance to swollen Q_{II}^G -Gyroid and Q_{II}^D -Diamond structures – pointing to the possibility of experimental misidentification. Our simulation method (the same that is described in refs.^{37,63}, see appendix A) is based on fast Fourier transform of voxelised representations; it is validated by demonstrating good agreement between the simulated **3etc**(187,193) structure and the experimental scattering pattern for the IBN-9 mesoporous silicate phase reported in ref.⁴³.

Figure 15 (a) shows the simulated scattering pattern of the **3etc**(187,193) structure close to the experimental parameters for the **3etc**(187,193) silica structure observed by Han *et al.*⁴³. The red curve represents the scattering pattern

of the ideal highly ordered **3etc**(187,193) structure based on the idealised CMC-surfaces (i.e. perfectly-periodic and with all symmetries of the $P6_3/mcm$ space group), computed at a highly resolved discretization. Most of the allowed hkl reflections of the uncoloured space group $P6_3/mcm$ (No. 193 in²¹) are present (grey lines in the background) and resolved in the q -range of this high resolution voxel-based simulation. Peak overlap start does not start before about $q = 3\text{nm}^{-1}$. Decreasing the spatial resolution of the model structures brings the simulated scattering pattern, represented by the blue curve in Figure 15 (left), closer to the experimentally observed powder XRD pattern in Fig. 1b of reference⁴³; Several of the peaks can no longer be resolved individually. There is good agreement between these two scattering pattern, and thus our simulation corroborates their reported structure. There are three main differences:

First, asymmetric peak broadening at low q -values is observed in the experimental data set, which we assume stems from the beam profile of their instrument, and which we have not accounted for in the simulation.

Second, our simulation suggests that the experimentally indexed (120) peak has in fact very low intensity at this channel volume fraction, and is more likely to be the more intense, very close (121) reflection. However, this difference is subtle, and may also stem from the fact that our simulations are based on ideal CMC surfaces of structures with homogeneous wall densities rather than the real surfaces investigated experimentally.

Third, the first peak (010) was not observed experimentally. However, its calculated q -value of 0.821nm^{-1} (or a 2θ -value of 1.15° when using Cu_α) is very close to the low q -limit of a conventional diffractometer.

Figure 15 (b) shows the simulated scattering pattern of the **3etc**(187,193) structure at different lipid volume fractions ϕ_{BL} (corresponding to varying wall thicknesses). As expected, the reflections remain at the same q -position, as the symmetry and unit cell size remain unchanged. Their intensities, however, change significantly; This stems from changes in the form factor, that is, from the scattering of local domains in the structure. It is interesting that for example the intensity of the (010) peak, or the ratio between the (110) and (002), is so sensitive to the channel thickness, that they may well serve as an independent measure for it.

Figure 16 shows the simulated scattering pattern for the three different model structures **4srs***(24,208), **4srs**(5,133), and **3dia**(24,220), each at two different lipid volume fractions ϕ_{BL} . Like in the case of the **3etc**(187,193) structure discussed above, the intensities of hkl -reflections vary significantly with the bilayer volume fraction.

The scattering patterns and hkl indices of the **4srs***(24,208) and the **4srs**(5,133) structure appear to be very different at first sight. If the peaks were indexed according to the coloured instead of uncoloured symmetry (see Tab. 1), it would be more obvious that at equal channel size most of the peaks in these two structures come to lie at identical q -positions. The main difference between these two structures are the intensities of the peaks, and the fact that the **4srs**(5,133) has additional peaks due to symmetry lowering from cubic to tetragonal. These additional peaks of the **4srs**(5,133) structure are the (211), (210) and (321), marked in red in Figure 16 (b).

It is interesting to note that the scattering pattern of the **4srs***(24,208) struc-

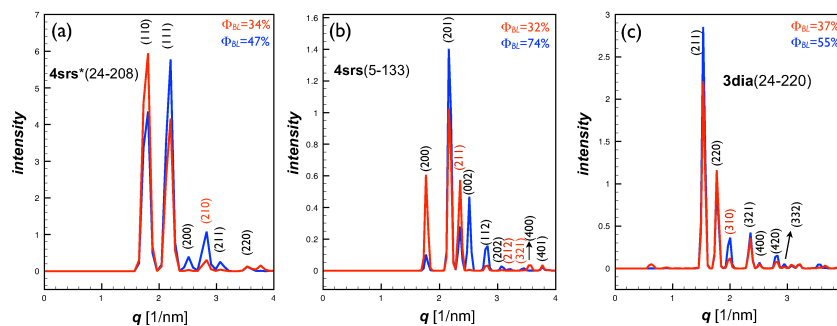


Fig. 16 Simulated scattering pattern at two different volume fractions of (a) the chiral **4srs***(24,208) structure (space group $P4_232$ with $a = 5\text{nm}$), (b) the achiral **4srs**(5,133) structure (space group $P4_2/nbc$ with $a = 10/\sqrt{2}\text{nm}$ and $c = 5\text{nm}$), and (c) the **3dia**(24,220) structure (space group $I\bar{4}3d$ with $a = 10\text{nm}$). The lattice parameters were chosen such that their uncoloured unit cells have the same cubic box of size 10nm .

ture has resemblance to that of a conventional bicontinuous cubic Diamond structure Q_{II}^D , frequently experimentally observed in soft matter, also as the AMS-10 mesoporous silica structure^{74–76}. The only feature present in the **4srs***(24,208) pattern that would unambiguously rule out its identification as the pattern of a conventional diamond structure is the (210) reflection, marked with red in Figure 16 (a). This reflection is forbidden for the conventional diamond structure (symmetry $Pn\bar{3}m$, see Tab. 1). However, it may also have low intensity or be absent for the **4srs***(24,208) structure, particularly at low lipid volume fractions ϕ_{BL} .

The case is similar for the scattering pattern of the **3dia**(24,220)-structure depicted in Figure 16(c). Most hkl -reflections and roughly also the intensities are in agreement with the conventional bicontinuous cubic gyroid Q_{II}^G , **2srs**(214,230) symmetry $Ia\bar{3}d$. The only hkl -reflection (which may or may not be of significant intensity in the **3dia**(24,220) pattern) that distinguishes the **3dia**(24,220) structure from the conventional gyroid structure is the (310) peak, which is forbidden for the space group $Ia\bar{3}d$.

We even expect the lattice parameters of these two polycontinuous geometries –misinterpreted as bicontinuous cubic phases– to differ only slightly from typical values for the bicontinuous Q_{II}^G and Q_{II}^D phases: Based on the same water content and normalised to constant area/volume, the apparent lattice parameter of a **3dia**(24,220), mis-interpreted as Q_{II}^G , and a **4srs***(24,208), mis-interpreted as Q_{II}^D , would only be enlarged by $\approx 30\%$. An estimate based on the same water content and normalised bilayer thickness would only make them appear $\approx 30\%$ and $\approx 10\%$ larger, respectively.

The apparent lattice parameter would be even further reduced if the phases contained less water. This is not unlikely, if we consider that the polycontinuous structures have significantly smaller variations of bilayer width at smaller water content (Fig. 11).

Concluding Remarks

The polymorphism of lipids and related soft matter systems has continuously witnessed the emergence of ever new spatial structures, all formed by spontaneous self-assembly of suitably designed molecules. First came micelles in water, then the neat and middle phases (lamellar and hexagonal phases), then Luzzati's bicontinuous Q_I^G Gyroid phase⁷⁷, then inverse bicontinuous phases including Q_{II}^G (ref.⁵), Q_{II}^P and Q_{II}^D , then inverse micellar FCC phases⁶¹, then inverse hexagonal micellar phases⁶⁶. While some of these geometries were identified without prior knowledge or expectation of a geometric model (such as Luzzati's initial findings of Q_I^G ⁷⁷), in many instances an awareness of the structural model was crucial for its identification in the experimental system.

The purpose of this article is to raise awareness of the geometric possibility of a new class of network-like mesophase geometries (of type II), termed polycontinuous; these consist of three or more aqueous network-like domains separated by a lipid bilayer that is branched, similarly to the inverse hexagonal or inverse micellar phases. We have here discussed specifically the tricontinuous **3etc**(187,193) and **3dia**(24,220) geometries and the tetracontinuous **4srs***(24,208) and **4srs**(5,133) geometries; this choice does, however, by no means imply that other structures with three or more interthreaded networks are not equally or more suited.

For example, the tricontinuous structure families **3pcu**(160,162), **3qtz**(145,180) and **3dia**(109,141) with varying *c/a*-ratio (that have been suggested as geometries for star-shaped molecules with mutually immiscible arms²⁹), or the tricontinuous **3gra**(10,192) and octacontinuous **8srs**(1,211) structure (that emerge from projections of hyperbolic forests onto periodic minimal surfaces^{25,26,28,32}) are relevant. There are more examples, many of which - in addition to the structures discussed above - are also listed by the reticular chemistry structure resource²² (www.rcsr.anu.edu.au): the tricontinuous family (with varying *c/a* ratio) of the **eta-c3** and **twt-c3** ($P6_2/22$), the tetracontinuous **dia-c4** ($P4/nbm$), **eta-c4** ($P6_222$), **qtz-c4** ($P6_222$) and **pcu-c4** ($P4_332$), and the hexacontinuous **dia-c6** ($P4_2/nmm$), **qtz-c6** ($P6_222$).

It appears highly unlikely that these polycontinuous phases be found in the well-studied phase diagrams of simple lipids in binary mixtures with water. However, we have here argued that both in terms of typical shape (Figs. 9 and 10) and in terms of packing frustration and homogeneity (Figs. 11 and 12) the difference between the molecular geometries that are likely to form the polycontinuous cases and existing molecular architectures are small; hence, there is no fundamental *geometric* reason that should prevent the formation of these phases in systems that are similar to existing lipids. Therefore, we suggest to search for systems where these phases form, by clever chemical design of the surfactant molecules themselves or of other system parameters (molecular polydispersity, addition on oil, proteins, silica precursor, solvents or co-surfactants). Some guidance for this design process may come from the experimental observation of the **3etc**(187,193) structure in mesoporous silicates^{18,43}, in particular also based on the simple CTAB surfactant¹⁸.

This article has addressed the formation energetics of reverse (type-II) phases, where variations of the local branched bilayer shape relate to stretching and bend-

ing. Our focus on reverse phases should by no means exclude the possibility of polycontinuous direct phases (of type I) with hydrophobic network domains separated by an aqueous matrix. A geometric analysis in terms of s and d of the equivalent direct structures is straight-forward, but its relevance to the self-assembly mechanism less immediate. For example, variations of the packing parameter of the hydrophobic domain, say a network domain of a single **srs** net bounded by a CMC surface, provides no insight into why Luzzati's Q_I^G phase –consisting in two such **srs** domains– can form, but not a phase consisting in a single **srs** network surrounded by water[‡]. Similarly, as long as three or four identical copies of a hydrophobic network domain can be intergrown without overlap and as long as interactions across the aqueous matrix are neglected, the simple geometric packing analysis of this article cannot distinguish between a phase based on 1, 2, 3 or 4 hydrophobic domains. However, if entropy or forces favour the formation of a homogeneous shape of the aqueous matrix, the analysis of this article is relevant also to the corresponding direct (type I) phases.

Several of the known polycontinuous geometries are spatially chiral. Out of the geometries discussed here only the **4srs***(24,208) is chiral, consisting of four equal-handed **srs** nets, but several other chiral polycontinuous geometries are known, such as the **3qtz**(145,180)-family, the **8srs**(1,211), and in fact also all interthreaded geometries based on the chiral **eta**, **qtz** and **twt**-net mentioned above. The homogeneity of the **4srs***(24,208) in terms of the molecular shape parameter Δs is very close to the bicontinuous Q_{II}^G phase and in terms of the bilayer width variations only slightly higher than the cubic inverse micellar phase. Considering these geometric constraints, it is conceivable that a self-assembly process could be designed that favours the formation of the **4srs***(24,208); the result would be a chiral structure with potentially striking optical properties including discrimination between light of different circular polarisation⁸². How the molecular geometry needs to be adapted to yield this result, and whether this necessarily involves chiral constituent molecules, is a question for future analysis, most likely by simulation.

The polycontinuous geometries described here, some of an innately beautiful visual appearance, should provide chemistry with inspirational design ideas for self-assembly. Surely, the assertion attributed to the Greek playwright Euripides (\approx 400 BC) that “*Mighty is geometry; joined with art, resistless.*” equally applies to the combination of geometry and chemistry.

Acknowledgements

We are indebted to Christophe Oguey for inspiration and practical help on various aspects of tricontinuous branched minimal surfaces, and in particular for the design of the **3dia**(24,220)structure. We are grateful to Kenneth Brakke for his *Surface Evolver* package, and for help with setting up a symmetry constraint

[‡] A single **srs** phase (of chiral symmetry $I4_132$) has been observed in some hard biological systems such as the porous chitin structure in the wing-scales of some butterfly species^{78–80}, where it is presumably templated from a biological cubic membrane (of achiral symmetry $Ia\bar{3}d$) at a length scale of approximately $a = 300 - 350$ nm significantly larger than in lipid systems. Neither in a synthetic liquid crystalline lipid/water system nor in a biological cubic membrane⁸¹ has a single **srs** phase yet been observed.

for the **3etc**(187,193) structure. We thank Toen Castle for comments and corrections of the manuscript. GEST and SCK acknowledge financial support by the Deutsche Forschungsgemeinschaft (DFG) under grant SCHR-1148/2-1 and by the German Academic Exchange Service (DAAD) through a joint program with the Australian Group-of-Eight universities. LDC, TV and STH gratefully acknowledge support from the Australian Research Council through the Discovery Projects scheme. MEE is funded by the DFG through grant SCHR1148/3, awarded as part of the DFG-Forschergruppe “Geometry and Physics of Spatial Random Systems”.

References

- 1 V. Luzzati, *Biological Membranes*, Academic Press (London), 1968, pp. 71–123.
- 2 V. Luzzati, A. Tardieu, T. Gulik-Krzywicki, E. Rivas and F. Reiss-Husson, *Nature (London)*, 1968, **220**, 485–488.
- 3 L. Scriven, *Nature*, 1976, **263**, 123–125.
- 4 K. Larsson, *Nature*, 1983, **304**, 664.
- 5 S. Hyde, S. Andersson, B. Ericsson and K. Larsson, *Z. Kristall.*, 1984, **168**, 213–219.
- 6 K. Larsson, *Journal of Colloid and Interface Science*, 1986, **113**, 299–300.
- 7 K. Fontell, *Colloid Polym. Sci.*, 1990, **268**, 264–285.
- 8 A. Schoen, *Infinite Periodic Minimal Surfaces without Self-Intersections*, NASA Technical Note TN D-5541, 1970.
- 9 H. Schwarz, *Gesammelte Mathematische Abhandlungen. 2 Bände.*, Springer, Berlin, 1890.
- 10 J. M. Seddon, J. Robins, T. Gulik-Krzywicki and H. Delacroix, *Phys. Chem. Chem. Phys.*, 2000, **2**, 4485–4493.
- 11 A. Fogden and S. T. Hyde, *Eur. Phys. J. B*, 1999, **7**, 91–104.
- 12 S. T. Hyde, Colloque de Physique C7-1990, 1990, pp. 209–228.
- 13 G. E. Schröder, S. Ramsden, A. Christy and S. T. Hyde, *Eur. Phys. J. B*, 2003, **35**, 551–564.
- 14 G. E. Schröder-Turk, A. Fogden and S. T. Hyde, *Eur. Phys. J. B*, 2006, **54**, 509–524.
- 15 W. Helfrich, *Z. Naturforsch.*, 1973, **28c**, 693–703.
- 16 D. Anderson, S. Gruner and S. Leibler, *PNAS*, 1988, **85**, 5364–5368.
- 17 P. Duesing, R. Templer and J. Seddon, *Langmuir*, 1997, **13**, 351–359.
- 18 Y. Zhao, L. Zhao, G. Wang and Y. Han, *Chem. Mater.*, 2011, **23**, 5250–5255.
- 19 K. Grosse-Braukmann, *Journal of Colloid and Interface Science*, 1997, **187**, 418–428.
- 20 G. Shearman, B. Khoo, M. Motherwell, K. Brakke, O. Ces, C. Conn, J. Seddon and R. Templer, *Langmuir*, 2007, **23**, 7276–7285.
- 21 *International Tables For Crystallography*, ed. T. Hahn, Kluwer Academic Publishers, Dordrecht, 1992.
- 22 M. O’Keeffe, M. Peskov, S. Ramsden and O. Yaghi, *Accts. Chem. Res.*, 2008, **41**, 1782–1789.
- 23 *Reticular Chemistry Structure Resource: www.rcsr.anu.edu.au*.
- 24 N. L. Rosi, J. Kim, M. Eddaoudi, B. Chen, M. O’Keeffe and O. M. Yaghi, *J. Am. Chem. Soc.*, 2005, **127**, 1504–1518.
- 25 S. T. Hyde and S. Ramsden, *Europhys. Lett.*, 2000, **50**, 135–141.
- 26 S. T. Hyde and C. Oguey, *Eur. Phys. J. B*, 2000, **16**, 613–630.
- 27 S. T. Hyde, S. J. Ramsden, T. Di Matteo and J. Longdell, *Solid State Sciences*, 2003, **5**, 35–45.
- 28 S. T. Hyde and G. E. Schröder, *Curr. Opin. Colloid Interface Sci.*, 2003, **8**, 5–14.
- 29 S. T. Hyde, L. Di Campo and C. Oguey, *Soft Matter*, 2009, **5**, 2782–2794.
- 30 V. Elser, *Philos. T. Math. Phys. Engin. Sci.*, 1996, **354**, pp. 2071–2075.
- 31 A. Wells, *Three-Dimensional Nets and Polyhedra*, Wiley & Sons, New York, 1977.
- 32 M. E. Evans, *Ph.D. thesis*, Australian National University, 2011.
- 33 S. J. Ramsden, V. Robins and S. T. Hyde, *Acta Cryst. A*, 2009, **65**, 81–108.
- 34 S. Okamoto, H. Hasegawa, T. Hashimoto, T. Fujimoto, H. Zhang, T. Kazama, A. Takano and Y. Isono, *Polymer*, 1997, **38**, 5275–5281.

-
- 35 N. Hadjichristidis, H. Iatrou, M. Pitsikalis, S. Pispas and A. Avgeropoulos, *Progress in Polymer Science*, 2005, **30**, 725–782.
- 36 Y. Matsushita, A. Takano, K. Hayashida, T. Asari and A. Noro, *Polymer*, 2009, **50**, 2191–2203.
- 37 L. de Campo, T. Varslot, M. J. Moghaddam, J. J. K. Kirkensgaard, K. Mortensen and S. T. Hyde, *Phys. Chem. Chem. Phys.*, 2011, **13**, 3139–3152.
- 38 K. Hayashida, A. Takano, T. Dotera and Y. Matsushita, *Macromolecules*, 2008, **41**, 6269–6271.
- 39 C.-I. Huang, H.-K. Fang and C.-H. Lin, *Phys. Rev. E*, 2008, **77**, 031804.
- 40 J. J. K. Kirkensgaard, *Phys. Rev. E*, 2012, **85**, 031802.
- 41 J. J. K. Kirkensgaard and S. Hyde, *Phys. Chem. Chem. Phys.*, 2009, **11**, 2016–2022.
- 42 X. Zeng, G. Ungar and M. Imperor-Clerc, *Nat Mater*, 2005, **4**, 562–567.
- 43 Y. Han, D. Zhang, L. Chng, J. Sun, L. Zhao, X. Zou and J. Ying, *Nat. Chem.*, 2009, **1**, 123–127.
- 44 Y. Zhao, D. Zhang, L. Zhao, G. Wang, Y. Zhu, A. Cairns, J. Sun, X. Zou and Y. Han, *Chem. Mater.*, 2011, **23**, 3775–3786.
- 45 D. Zhang, J. Sun, Y. Han and X. Zou, *Microporous and Mesoporous Materials*, 2011, **146**, 88–96.
- 46 J. Beck, J. Vartuli, W. Roth, M. Leonowicz, C. Kresge, K. Schmitt, C. Chu, D. Olson and E. Sheppard, *J. Am. Chem. Soc.*, 1992, **114**, 10834–10843.
- 47 C. Kresge, M. Leonowicz, W. Roth, J. Vartuli and J. Beck, *Nature*, 1992, **359**, 710–712.
- 48 V. Alfreðsson and M. Anderson, *Chem. Mater*, 1996, **8**, 1141–1146.
- 49 A. Monnier, F. Schth, Q. Huo, D. Kumar, D. Margolese, R. S. Maxwell, G. D. Stucky, M. Krishnamurthy, P. Petroff, A. Firouzi, M. Janicke and B. F. Chmelka, *Science*, 1993, **261**, 1299–1303.
- 50 X. Auvray, C. Petipas, R. Anthore, I. Rico and A. Lattes, *J. Phys. Chem.*, 1989, **93**, 7458–7464.
- 51 S. T. Hyde, S. Andersson, K. Larsson, Z. Blum, T. Landh, S. Lidin and B. Ninham, *The Language of Shape*, Elsevier Science, Amsterdam, 1st edn., 1997.
- 52 J. Israelachvili, D. Mitchell and B. Ninham, *J. Chem. Soc. Faraday Trans. 2*, 1976, **72**, 1525–1568.
- 53 D. Mitchell and B. Ninham, *J. Chem. Soc. Faraday Trans. II*, 1981, **77**, 601–629.
- 54 J. Sadoc and J. Charvolin, *J. Phys. France*, 1987, **48**, 1559–1569.
- 55 B. Ninham and P. Lo Nostro, *Molecular Forces and Self Assembly: In Colloid, Nano Sciences and Biology*, Cambridge University Press, 2010.
- 56 U. Schwarz and G. Gompper, *Morphology of Condensed Matter*, Springer, 2002, pp. 107–151.
- 57 J. Charvolin and J. Sadoc, *Colloque de Physique C7-1990*, 1990, pp. 83–96.
- 58 A. Fogden, S. T. Hyde and G. Lundberg, *J. Chem. Soc. Faraday Trans.*, 1991, **87**, 949–955.
- 59 U. Schwarz and G. Gompper, *Langmuir*, 2001, **17**, 2084–2096.
- 60 G. E. Schröder-Turk, A. Fogden and S. T. Hyde, *Eur. Phys. J. B*, 2007, **59**, 115–126.
- 61 J. M. Seddon, N. Zeb, R. H. Templer, R. N. McElhaney and D. A. Mannock, *Langmuir*, 1996, **12**, 5250–5253.
- 62 G. E. Schröder, S. Ramsden, A. Fogden and S. T. Hyde, *Physica A*, 2004, **339**, 137–144.
- 63 G. E. Schröder-Turk, V. Trond, L. D. Campo, S. C. Kapfer and W. Mickel, *Langmuir*, 2011, **27**, 10475–10483.
- 64 H. Blum, *J. Theor. Biol.*, 1973, **38**, 205–287.
- 65 *Medial Representations: Mathematics, Algorithms and Applications*, ed. K. Siddiqi and S. Pizer, Springer, 2007.
- 66 G. Shearman, A. Tyler, N. Brooks, R. Templer, O. Ces, R. Law and J. Seddon, *J. Americ. Chem. Soc.*, 2009, **131**, 1678–1679.
- 67 A. Schoen, *J. Roy. Soc. Interf. Focus*, ??, ??, ??
- 68 S. T. Hyde, *Handbook of Applied Surface and Colloid Chemistry*, John Wiley & Sons, Ltd, 2001, pp. 299–332.
- 69 P. M. Duesing, J. M. Seddon, R. H. Templer and D. A. Mannock, *Langmuir*, 1997, **13**, 2655–2664.
- 70 M. Doi and T. Ohta, *J. Chem. Phys.*, 1991, **95**, 1242–1248.
- 71 S. C. Kapfer, S. T. Hyde, K. Mecke, C. H. Arns and G. E. Schröder-Turk, *Biomaterials*, 2011, **32**, 6875–6882.
- 72 S. Nachtrab, S. C. Kapfer, C. H. Arns, M. Madadi, K. Mecke and G. E. Schröder-Turk, *Adv. Mater.*, 2011, **23**, 2633–2637.
- 73 S. Nachtrab, S. C. Kapfer, D. Rietzel, D. Drummer, M. Madadi, C. H. Arns, A. M. Kraynik, G. E. Schröder-Turk and K. Mecke, *Adv. Eng. Mater.*, 2012, **14**, 120–124.

- 74 C. Gao, Y. Sakamoto, K. Sakamoto, O. Terasaki and S. Che, *Angew. Chem. Int. Edit.*, 2006, **45**, 4295–4298.
- 75 A. E. Garcia-Bennett, C. Xiao, C. Zhou, T. Castle, K. Miyasaka and O. Terasaki, *Chem.-Eur. J.*, 2011, **17**, 13510–13516.
- 76 K. Miyasaka, A. Garcia Bennett, L. Han, Y. Han, C. Xiao, N. Fujita, T. Castle, Y. Sakamoto, S. Che and O. Terasaki, *Interface Focus*, 2012.
- 77 V. Luzzati and P. Spegt, *Nature*, 1967, **215**, 701–704.
- 78 K. Michielsen and D. Stavenga, *J. R. Soc. Interface*, 2008, **5**, 85–94.
- 79 V. Saranathan, C. Osuji, S. Mochrie, H. Noh, S. Narayanan, A. Sandy, E. Dufresne and R. Prum, *PNAS*, 2010, **107**, 11676–11681.
- 80 G. Schröder-Turk, S. Wickham, H. Averdunk, M. Large, L. Poladian, F. Brink, J. Fitz Gerald and S. T. Hyde, *J. Struct. Biol.*, 2011, **174**, 290–295.
- 81 Z. A. Almshergqi, T. Landh, S. D. Kohlwein and Y. R. Deng, *Int. Rev. Cel. Mol. Biol.*, 2009, **274**, 275–342.
- 82 M. Saba, M. Thiel, M. Turner, S. T. Hyde, M. Gu, K. Grosse-Brauckmann, D. Neshev, K. Mecke and G. E. Schröder-Turk, *Phys. Rev. Lett.*, 2011, **106**, 103902.
- 83 K. Brakke, *Exper. Mathem.*, 1992, **1**, 141–165.
- 84 N. Amenta, B. Marshall and M. Kamvysselex, Proceedings of SIGGRAPH 98, 1998.
- 85 N. Amenta, S. Choi and R. Kolluri, *Computational Geometry: Theory and Applications*, 2001, **19**, 127–153.
- 86 A. Guinier, *X-ray diffraction in crystals, imperfect crystals and amorphous bodies*, Dover, New York, 1994.
- 87 K. Schmidt-Rohr, *J. Appl. Crystallogr.*, 2007, **40**, 16–25.

A Numerical Methods

Constant mean curvature surfaces by Surface Evolver

Triangulated approximations of constant mean curvature (CMC) surfaces that are here used as models for the head group surfaces bounding the aqueous network-like domains are obtained by *Surface Evolver*⁸³; this program performs iterative minimisation of surface forms with respect to different surface functionals, by gradient methods applied to triangulated surface representations.

The CMC network domains used for the **srs** based geometries (i.e. for **4srs***(24,208), **4srs**(5,133) and the bicontinuous Gyroid's **2srs**(214)) are obtained by the method described in ref.¹⁹. The initial triangulation is a periodic body consisting of 96 triangular facets that is topologically equivalent to a CMC body around a single **srs** net within the primitive unit cell (with lattice vectors (1,0,0), (0,1,0) and (1/2,1/2,1/2)), implemented using Surface Evolver's TORUS model; each of the four network vertices is represented by a body of 24 triangular facets with four "open" rectangular facets along which it connects to the adjacent vertices; the vertices and edges of this initial configuration fulfil all symmetries of the space group $I4_132$ of the single **srs** network. Through a sequence of steps of the conjugate gradient and Hessian methods interspersed with mesh refinement, the shape of the body is evolved to minimise the discrete version of the functional $E[S] := \int_S (H(\mathbf{x}) - h_0)^2 dA$ with h_0 the desired mean curvature value, the point-wise mean curvature $H(\mathbf{x})$ is discretized using the Surface Evolver method `star_normal_sq_mean_curvature` using `linear` elements. Remeshing steps consist in refinement of the triangulation (`r` in Surface Evolver; division of each edge into two edges and each triangle into four smaller ones), equiangulation (`u`; topological transition between two adjacent triangles to reach more even triangle angles), vertex averaging (`V`; replacement of vertex coordinates with average coordinates of the first shell neighbourhood) and removal of short edges (`t`; with a cut-off chosen relative to average edge length). Symmetries are not explicitly constrained during the evolution towards constant mean curvature. However, the symmetries of the initial triangulation are found to be maintained, giving CMC surfaces with the desired $I4_132$ symmetry. The **4srs***(24,208), **4srs**(5,133) and Q_{II}^G data in Figs. 9 to 12 are calculated from triangulations with approximately 24500 triangles per primitive unit cell per the single **srs** CMC body.

The CMC surfaces bounding the aqueous domains of the **3etc**(187,193) structures are obtained by the setup demonstrated in Fig. 17. A surface patch bounded by mirror planes is minimised with respect to the same functional $E[S]$ as above, with an additional symmetry constraint (`symmetry_group` 'rotate') to ensure the perpendicular two-fold rotation symmetry (blue line in Fig. 17). The sequence of steps used for this minimisation is similar to those described for the **srs** CMC surfaces (in

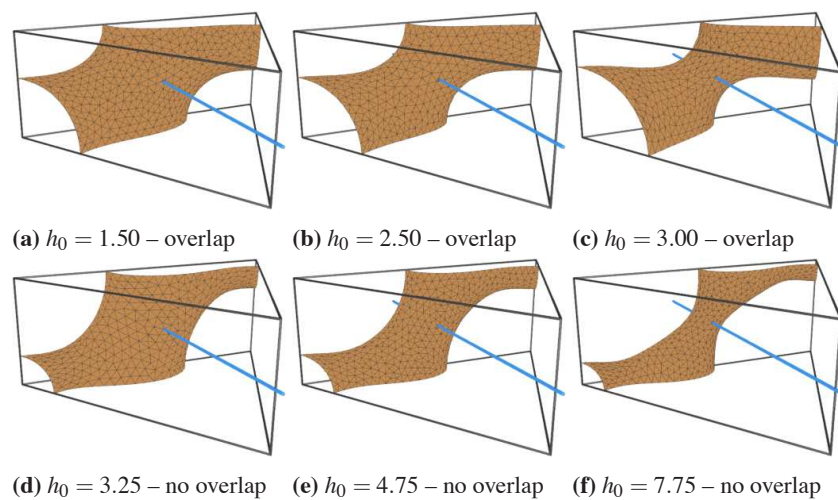


Fig. 17 CMC surface patches for a single **etc** network domain as function of the mean curvature h_0 , for fixed $c/a = 0.79$ and $a = 1$ in space group $P6_3/mcm$, as used for the evaluation in Surface Evolver. Out of convenience for the Surface Evolver setup, this six-sided patch that is bounded by mirror-planes is used; it has an internal two-fold symmetry (blue line) perpendicular to the surface (enforced in the Surface Evolver calculation using the keyword `symmetry_group rotate`) and it is therefore not the asymmetric patch. The bounding box is the equilateral prism with height $c/2$ and triangular edge length $a/\sqrt{3}$ (c and a refer to the values of the uncoloured space group $P6_3/mcm$ of the **3etc**(187,193) structure). The **3etc**(187,193) structure is obtained by application of $\pm 120^\circ$ rotations around the vertical line through the centre points of the prism. When varying the parameter h_0 for fixed c/a we find that a critical value of h_c exists ($h_c = 3.15 \pm 0.15$ for $c/a = 0.79$ and $a = 1$) where the shape of the CMC surface changes discontinuously as function of h_0 ; this occurs between (c) and (d). Note the bulkier regions near the prism vertices for $h_0 < h_c$ (see a-c), that abruptly become much narrower when $h_0 > h_c$ (see d-f). For $h_0 < h_c$, the CMC surfaces do not lead to non-overlapping **3etc**(187,193) configurations and are hence irrelevant for lipid self-assembly. For $h_0 > h_c$, the corresponding **3etc**(187,193) configurations are non-overlapping and hence valid lipid bilayer configurations. At h_c , the CMC domains are not in contact, i.e. $d_{min}(h) = \min_{p \in S} d(p)$ is greater than 0 at h_c . We observe a qualitatively similar trend also for $c/a = 0.95$ and $c/a \approx 1.1$. See Tab. 2 for approximate values of h_0 .

addition, we have observed improved convergence if a few initial conjugate gradient steps are applied to the coarse patch with the surface area functional $A[S] := \int_S dA$ rather than $E[S]$ as the functional to minimise). Note the discontinuous dependence of the resulting surface shape as a function of the mean curvature value h_0 discussed in Fig. 17; whether this discontinuity corresponds to a bifurcation with two solutions to the problem (such as is observed for the CMC Gyroid surfaces in ref.¹⁹ for high enough values of h_0) is to be addressed by future studies. The structural data for **3etc**(187,193) phases in Figs. 9 to 14 is based on triangulations with 1500 to 6500 points for the patch shown in Fig. 17.

Data for the **3dia**(24,220) structures in this article is preliminary, in that a proper convergence analysis of the structure has not been performed and in that we only investigated one value of ϕ_{BL} . The surface triangulation is obtained by the method described in ref.²⁹, by minimising the area $A[S]$ subject to a volume constraint. An equivalent approach to that used for **srs** and **etc** structures is equally possible.

Bilayer mid-surfaces by Medial Surface Construction

Medial surfaces are computed by a Voronoi-based algorithm, first described by Amenta *et al.*^{84,85} and adapted specifically to minimal surface geometries in refs.^{13,14}. This algorithm takes a triangulation of the surface S by n vertices x_i connected by triangles as input ($i = 1, \dots, n$), computes the Voronoi cells of all vertices x_i of the triangulation, and approximates the medial surface point $\text{ms}(x_i)$ as the so-called *pole*⁸⁵; the pole is that vertex y_p of the set of vertices $\{y_i\}$ of the Voronoi cell of x_i that maximises the distance $(y_i - x_i) \cdot N(x_i)$ to x_i where $N(x_i)$ is the surface normal at vertex x_i and \cdot the scalar product. Medial surface algorithms of this type are plagued by noise-sensitivity in places where $d(p) \approx 1/\kappa(p)$ where $1/\kappa(p)$ is the reciprocal of one of the principal curvatures and where simultaneously $\kappa(p) > 0$ (i.e. curvature towards the normal). For the cases studied in this article –inverse polycontinuous phases– the bilayer “width” $2d(p)$ is typically much smaller than the interface’s curvatures, hence largely alleviating these noise sensitivity issues.

Simulated SAXS scattering patterns

Simulated small angle scattering (SAXS) patterns of the predicted polycontinuous phases are determined with the voxel-based Fourier method described in refs.^{37,63}, based on the principles described in ref.⁸⁶. The following description is adapted from ref.⁶³. Our analysis is based on a voxelized representation of the branched bilayer. A two-phase scattering model is used where constant scattering length density values ρ_{BL} and ρ_{AQ} are assigned to the branched bilayer and its complement (the aqueous labyrinth-like compartments), respectively. For the case of the hexagonal mesophases based on the **3etc**(187,193) structure, the bilayer is discretized on a rectangular grid of size $\sqrt{3}a \times a \times c$. This grid represents a translational (but not primitive) unit cell of the hexagonal space group (lattice vectors are [100], [-110] and [001]). The X-ray scattering density of the points inside the bilayer is ρ_{BL} ; for the remaining grid points representing the aqueous domains $\rho = \rho_{AQ}$. We can, without loss of generality, assume that the mean scattering density is 0, as deviations from this will only contribute to the scattering curve at $q = 0$ (forward scattering). For a two-phase system, linearity of the Fourier transform therefore implies that both the absolute values ρ_{AQ} and ρ_{BL} and also their ratio ρ_{AQ}/ρ_{BL} only affect the scattering function by a constant factor, and do not alter the peak locations or relative intensities. The numerical value is therefore irrelevant for our analysis. From the voxelized representations of the mesophase SAXS scattering curves are determined by Fast Fourier Transform (FFT) using an approach which is based on that presented in Schmidt-Rohr (see ref.⁸⁷). Using the FFT to compute the Fourier transform, we inherently assume that the computational grid is a rectangular lattice. This leads to some complications with respect to our discretization: by discretizing a structure with hexagonal symmetries, we invariably introduce discretization errors. These errors do not obey the symmetries of the original structure, but are rather forced onto the rectangular grid used for the computations. As a result they lead to additional peaks corresponding to symmetries of the computational grid.

To break the symmetries of the discretization, we introduce random permutations of ρ_{BL} and ρ_{AQ} for the voxels that lie at the interface between the aqueous channels and the bilayer. On the one hand, this ensures that an error which is present in one cell does not persist periodically across the computational domain, and therefore does not contribute additional peak values in the resolved spectra. On the other hand, this emulates random imperfections/roughness at the interface between the aqueous channels and the bilayer. As a consequence, simulations using model structures with a higher spatial resolution (high number of voxels) will represent scattering from a structure which has less imperfections, and therefore is relatively smoother than those of a lower spatial resolution.

B Appendix C: Expressions for Δs and Δd for H_{II} and Q_{II}^{227}

All geometric properties of the inverse hexagonal columnar and the FCC inverse micellar phase can be expressed analytically. For the face-centered cubic (FCC) configuration of spherical micelles and the hexagonal configuration of parallel cylinders, we find expressions of the scaled mean curvature $H/(A/V)$, the medial surface distance d and the shape parameter s , respectively. The angle dependence, the mean value and the weighted standard deviation of d and s are calculated and compared with the numerically found values in figures 10, 12 and 11.

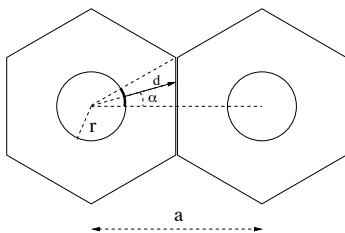


Fig. 18 Illustration of the hexagonal cylinder phase. Two cylinders (representing the aqueous compartments of the inverse hexagonal columnar phase) and their medial surfaces (inside the branched bilayer) are shown in a cross section perpendicular to the cylinder axes.

Hexagonal cylinder packings

The asymmetric unit of the hexagonal cylinder phase with lattice constant a and sphere radius r is a triangular prism of length with height L along the cylinder axes, see Fig. 18. The base triangle is rectangular with catheti of length $a/2$ and $a/\sqrt{6}$, corresponding to the angle $\pi/6$ at the centre of the sphere. The volume fraction of the aqueous network domain (i.e. inside of the cylinders) is given by:

$$\phi_{AQ} = V_{cyl}/V_{asy} = \frac{\frac{\pi}{12} r^2}{\frac{a^2}{8} \tan(\frac{\pi}{6})} = \frac{2\pi}{\sqrt{3}} \frac{r^2}{a^2} \quad (8)$$

with $\phi_{BL} = 1 - \phi_{AQ}$. The mean curvature of the cylinder is given by $H = (2r)^{-1}$. The surface area of the cylinder surface inside the asymmetric unit patch is given by $A = \pi r L / 6$ and the volume of the part of the asymmetric unit occupied by the matrix domain by $V = V_{asy} - V_{cyl}$. Hence, the scaled mean curvature can be expressed in terms of the volume fraction ϕ_{AQ} :

$$\frac{HV}{A} = \frac{1 - \phi_{AQ}}{4\phi_{AQ}} \quad (9)$$

The medial surface distance is expressed in terms of the polar angle α (cf. figure 18):

$$d(\alpha) = \frac{a}{2\cos\alpha} - r \quad (10)$$

Averages of a function $f(\alpha)$ in the asymmetric unit are given by:

$$\langle f(\alpha) \rangle = \frac{6}{\pi} \int_0^{\pi/6} d\alpha f(\alpha) \quad (11)$$

The average medial surface distance and its weighted standard deviation are hence given by:

$$\langle d \rangle = \frac{a}{2} \left\langle \frac{1}{\cos\alpha} \right\rangle - r = \frac{a}{2} \left(\frac{3\ln 3}{\pi} - 3^{(1/4)} 2^{(1/2)} \pi^{-(1/2)} \sqrt{\phi_{AQ}} \right) \quad (12)$$

$$\Delta d = \frac{a}{2} \sqrt{\langle \cos^{-2}\alpha \rangle - \langle \cos^{-1}\alpha \rangle^2} \quad (13)$$

$$\frac{\Delta d}{\langle d \rangle} = \frac{\sqrt{\langle \cos^{-2}(\alpha) \rangle - \langle \cos^{-1}(\alpha) \rangle^2}}{\frac{3\ln 3}{\pi} - 3^{(1/4)} 2^{(1/2)} \pi^{-(1/2)} \sqrt{\phi_{AQ}}} = \frac{\sqrt{2\sqrt{3}\pi - (3\ln 3)^2}}{3\ln 3 - (2\pi)^{(1/2)} 3^{(1/4)} \sqrt{\phi_{AQ}}} \quad (14)$$

The shape parameter is defined as the quotient of the infinitesimal matrix domain volume $\delta V(\alpha)$ and the product of the infinitesimal surface area $\delta A(\alpha)$ and the medial surface distance d . We obtain

$$\delta A(\alpha) = Lr\delta\alpha \quad (15)$$

$$\delta V(\alpha) = \delta V_{asy} - \delta V_{cyl} = L \frac{\delta\alpha}{2} \left[\left(\frac{a}{2\cos\alpha} \right)^2 - r^2 \right] \quad (16)$$

$$\Rightarrow s(\alpha) = \frac{\delta V}{\delta A d} = \frac{1}{2r} \left(\frac{a}{2\cos\alpha} + r \right) = \frac{1}{2} \left[1 + \sqrt{\frac{\pi}{2\sqrt{3}}} \cdot \frac{1}{\sqrt{\phi_{AQ}}} \cdot \frac{1}{\cos\alpha} \right] \quad (17)$$

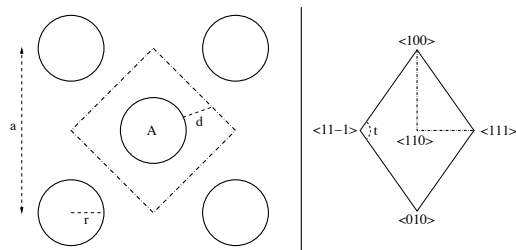


Fig. 19 FCC sphere packing illustration. Left: Sectional drawing of (100)-plane through the sphere origin. The cross section of the medial surface around sphere A is shown by a dashed line. Right: One of the faces of the medial surface (a rhombic dodecahedron). The obtuse angle t is the tetrahedral angle (i.e. $t \approx 109.5^\circ$). The dashed quarter of the rhombus forms the base of the asymmetric unit, a pyramid with its apex in the center of the dodecahedron.

with the average and the standard deviation:

$$\langle s \rangle = \frac{1}{2} \left[1 + \sqrt{\frac{\pi}{2\sqrt{3}\phi_{AQ}} \left\langle \frac{1}{\cos \alpha} \right\rangle} \right] = \frac{1}{2} \left[1 + \frac{3 \ln 3}{\sqrt{2\pi\sqrt{3}}} \cdot \frac{1}{\sqrt{\phi_{AQ}}} \right] \quad (18)$$

$$\Delta s = \frac{a}{r} \sqrt{\langle \cos^{-2} \alpha \rangle - \langle \cos^{-1} \alpha \rangle^2} = H \Delta d \quad (19)$$

$$\frac{\Delta s}{\langle s \rangle} = \frac{\sqrt{\langle \cos^{-2}(\alpha) \rangle - \langle \cos^{-1}(\alpha) \rangle^2}}{2^{(1/3)} 3^{(1/4)} \pi^{-(1/2)} \sqrt{\phi_{AQ}} + \langle \cos^{-1} \rangle} = \frac{\sqrt{2\pi - 3\sqrt{3} \ln^2(3)}}{\sqrt{2\pi} \sqrt{\phi_{AQ}} + 3^{(3/4)} \ln 3} \quad (20)$$

FCC packed spherical micelles

The FCC sphere packing with cubic lattice parameter a and sphere radius r is illustrated in figure 19. The asymmetric unit cell is a pyramid with a right-angled triangle as base, with its vertices at $a/4 \cdot (2, 0, 0)$, $a/4 \cdot (1, 1, 0)$, $a/4 \cdot (1, 1, 1)$, and the apex in the sphere centre (origin). The volume fraction of the network domain (i.e. the inside of the spheres) is given by

$$\phi_{AQ} = V_{sph}/V_{asy} = \frac{\frac{4}{3}\pi r^3}{\frac{1}{16}a^3} = \frac{16\pi}{3} \cdot \left(\frac{r}{a}\right)^3 \quad (21)$$

The mean curvature is $1/r$ and the part of the surface area of the sphere that is within the asymmetric unit patch is $A = \pi r^2/12$, yielding the scaled mean curvature for the matrix domain:

$$\frac{H}{A/V} = \frac{1 - \phi_{AQ}}{3\phi_{AQ}} \quad (22)$$

with the volume of the asymmetric unit that is occupied by the matrix domain $V = V_{asy} - V_{cyl}$. In the Cartesian system where $\langle 110 \rangle$ becomes zenith, the corner coordinates (for simplicity normalised by $4/a$) of the triangle transform like

$$\begin{aligned} (1, 1, -1) &\rightarrow (0, 1, \sqrt{2}) \\ (1, 1, 0) &\rightarrow (0, 0, \sqrt{2}) \\ (2, 0, 0) &\rightarrow (\sqrt{2}, 0, \sqrt{2}) \end{aligned} \quad (23)$$

The triangle can be parametrised in terms of the solid angle $\Omega = (\vartheta, \varphi)$ in the new coordinate system with the angles ϑ and φ defined by $\vec{r} = \rho(\sin \vartheta \cos \varphi, \sin \vartheta \sin \varphi, \cos \vartheta)$:

$$\begin{aligned} 0 &\leq \varphi \leq \frac{\pi}{2} \\ 0 &\leq \vartheta \leq \arctan\left(\frac{1}{\cos \varphi + \sqrt{2} \sin \varphi}\right) := \vartheta_{max}(\varphi) \end{aligned} \quad (24)$$

The average value of a function $f(\Omega)$ is obtained via:

$$\langle f(\Omega) \rangle = \frac{12}{\pi} \int_0^{\frac{\pi}{2}} d\varphi \int_0^{\vartheta_{\max}(\varphi)} d\vartheta \sin \vartheta f(\Omega) = \frac{12}{\pi} \int_0^{\frac{\pi}{2}} d\varphi \int_{\cos(\vartheta_{\max}(\varphi))}^1 du f(u, \varphi) \quad (25)$$

with the substitution $\cos(\vartheta) = u$ in the last identity.

The distance of a point on the medial surface to the origin of the corresponding sphere is determined by taking use of the fact that the z -coordinate is constant within the asymmetric surface patch:

$$\rho(\Omega) = \frac{a}{\sqrt{8}} \frac{1}{\cos \vartheta} \quad (26)$$

Medial surface distance, local surface area and local matrix domain volume can be expressed in terms of $\rho(\Omega)$:

$$d(\Omega) = \rho(\Omega) - r \quad (27)$$

$$\delta A(\Omega) = r^2 \cdot \delta \Omega = \text{const.} \quad (28)$$

$$\delta V(\Omega) = \frac{\delta \Omega}{3} (\rho^3(\Omega) - r^3) \quad (29)$$

Substituting $f(\phi_{AQ}) := \sqrt{8} \left(\frac{3}{16\pi}\right)^{(1/3)} \phi_{AQ}^{(1/3)}$ and using a partial fraction expansion, the shape parameter is decomposed into exponents of $u = \cos(\vartheta)$:

$$s(u) = \frac{\rho^3(u) - r^3}{3r^2(\rho(u) - r)} = \frac{1}{3f^2} \frac{u^{-3} - f^3}{u^{-1} - f} = \frac{1}{3} \{1 + (fu)^{-1} + (fu)^{-2}\} \quad (30)$$

Using the abbreviation $c_n := \langle u^{-n} \rangle$, we derive the average and standard deviation of the medial surface distance d

$$\langle d \rangle = \frac{a}{\sqrt{8}} (c_1 - f(\phi_{AQ})) \quad (31)$$

$$\Delta d = \frac{a}{\sqrt{8}} \sqrt{c_2 - c_1^2} \quad (32)$$

$$\frac{\Delta d}{\langle d \rangle} = \frac{\sqrt{c_2 - c_1^2}}{c_1 - f(\phi_{AQ})} \quad (33)$$

as well as the average and the standard deviation of the shape parameter s

$$\langle s \rangle = \frac{1}{3} \left\{ 1 + \frac{c_1}{f} + \frac{c_2}{f^2} \right\} \quad (34)$$

$$\Delta s = \frac{1}{3} \sqrt{\frac{c_2 - c_1^2}{f^2} + 2 \frac{c_3 - c_1 c_2}{f^3} + \frac{c_4 - c_2^2}{f^4}} \quad (35)$$

$$\frac{\Delta s}{\langle s \rangle} = \frac{\sqrt{\frac{c_2 - c_1^2}{f^2} + 2 \frac{c_3 - c_1 c_2}{f^3} + \frac{c_4 - c_2^2}{f^4}}}{1 + \frac{c_1}{f} + \frac{c_2}{f^2}} \quad (36)$$

with $f := f(\phi_{AQ})$. To obtain the numerical values of c_n , the integral defined in equation 25 has to be solved. While the inner integral over u is straight forward, the outer integral over φ is calculated numerically with Simpson's rule and 10^6 nodes in the interval $(0, \pi/2)$. The first eight digits of the numerical values of the constants are

$$f(\phi_{AQ}) = 1.1053389 \times (\phi_{AQ})^{1/3}, \quad (37)$$

$$c_1 = 1.1004937, \quad (38)$$

$$c_2 = 1.2163364, \quad (39)$$

$$c_3 = 1.3503394, \quad (40)$$

$$c_4 = 1.5060711. \quad (41)$$